Universität Münster

Spatially resolved gain measurements for CBM TRD MWPC production

Bachelorarbeit

Ruben Förster

Universität Münster

Institut für Kern- & Teilchenphysik

AG Andronic / Klein-Bösing

Eidesstattliche Erklärung

Hiermit versichere ich, *Ruben Förster*, dass ich die vorliegende Arbeit selbstständig verfasst und keine anderen als die angegebenen Quellen und Hilfsmittel verwendet habe. Gedanklich, inhaltlich oder wörtlich übernommenes habe ich durch Angabe von Herkunft und Text oder Anmerkung belegt bzw. kenntlich gemacht. Dies gilt in gleicher Weise für Bilder, Tabellen, Zeichnungen und Skizzen, die nicht von mir selbst erstellt wurden.

Münster, 10. Oktober 2023

_____

Ruben Förster

Contents

1 Introduction

Figure 1.1: Layout of the existing and planned facilities at the international *International Facility for Antiproton and Ion Research* (Fair). [1]

The *Compressed Baryonic Matter Experiment* (CBM) is an experiment that is under construction at the *International Facility for Antiproton and Ion Research* (FAIR) in Darmstadt, which is displayed in figure 1.1. Visible is the existing SIS18 synchrotron in blue. The SIS100 accelerator, which is currently beeing built, is displayed in red together with experimental and storage rings. New experiments are shown in black. The CBM experiment is one of these experiments currently under construction. The goal of the experiment is to study the phase diagram of nuclear matter at high baryon densities [2].

The experimental setup of CBM can be seen in figure 1.2. The experiment is a fixed target experiment, with a multitude of detectors being located behind the target allowing detection and tracking of different particles generated in the performed collisions. One of the detectors that is part of the CBM experiment is the TRD (Transition Radiation Detector). The detector serves for particle tracking and identification. It consists of four layers of Multiwire Proportional Chambers (MWPCs) behind a layer of radiators each.
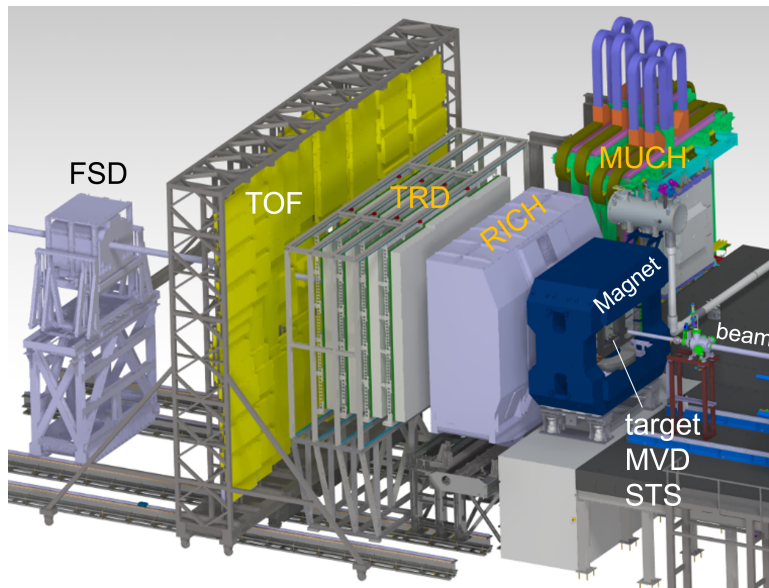
Figure 1.2: General Setup of the CBM Experiment with the beam entering the experimental hall on the right. The four layer TRD detector is shown in gray and green [3, slide 1]

As part of the development and construction of these chambers, spatially resolved gain measurements are to be performed, which will measure the homogeneity of the local signal amplification. The subject of this thesis is the automation of these gain scans and test measurements performed on an already existing chamber. This is done in preparation for series production, in which scans are performed on newly build chambers as they are finished.

2 Experimental Background

2.1 Interaction of γ-Radiation with Matter
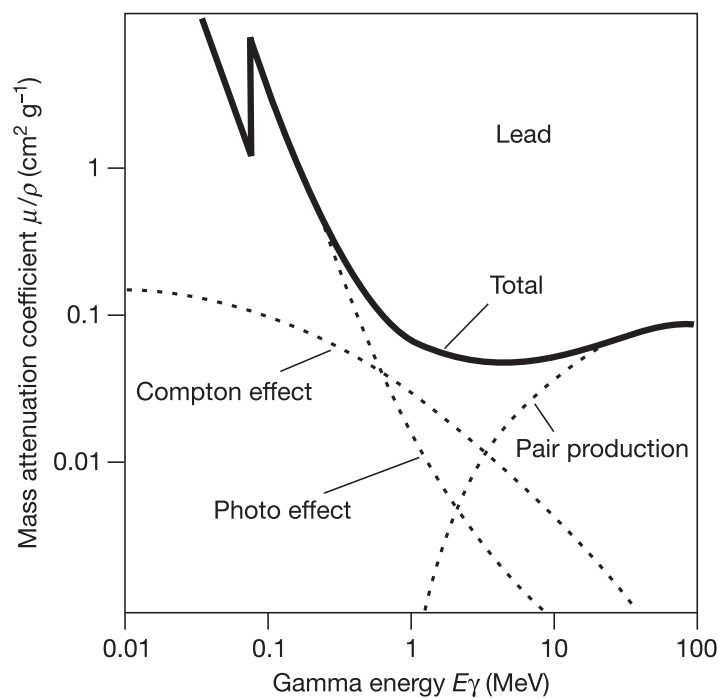
Figure 2.1: Graph showing contribution of the compton effect, the photo effect and pair production to the overall cross-section of lead at different photon energies. [4, p. 189]

When photons pass through any kind of detector, the mechanisms that govern the working principles and cross-section of the detector are described by how γ-radiation interacts with matter. The typical cross-section of a photon in matter can be found in figure 2.1. It can be differentiated between 3 main effects, [5, p. 86]:

The Photoelectric Effect describes the full absorption of an incoming photon by an electron of an inner shell of the atom. The electron leaves the atom with the energy $E_{kin} = h \cdot \nu - E_b$ [5, p. 87]. The energy of the photon $h \cdot \nu$ needs to be greater than the binding energy E_b. Since the photoelectric effect is dependent on the binding energy of the electron's, there are

discrete energies, where edges in the cross-section of the photoelectric effect can be observed. [5, p. 87]

Compton Scattering   describes inelastic scattering of the photon at an electron of an outer shell of an atom. The electron gets ejected out of the atom's shell, while the photon is redirected by an angle θ and loses some of its energy. [5, p. 86]

Pair Production   occurs when a photon with an energy $E_\gamma \geq 2m_e c^2$ causes the formation of an electron-positron-pair. The conversation of momentum dictates that this only happens when interacting with nukleus that then takes up the remaining momentum. [5, p. 87]

2.2 Gas filled Detectors

Gas detectors measure the ionization of gas inside the detector caused by incoming radiation. A schematic showing the design of a cylindrical gas detector can be found in figure 2.2. In the following experiment γ-radiation will enter the detector volume and create an initial charge, mainly through the photoelectric effect [6]. The resulting electrons and ions are accelerated by an electric field created by applying a voltage between the anode and cathode of the detector. The ions move towards the cathode, while the electrons move towards the anode, which consists of one or multiple wires. In the proximity to the anode wire the electric field increases in strength with $E(r) \sim U/r$ [7], due to the cylindrical symmetry of the field. Because of the acceleration, the electrons will gain enough energy to cause secondary ionizations causing secondary charges which will intern also experience acceleration by the electric field and lead to even more ionization, causing a chain reaction. Due to the inversely proportional change of the electric field this effect gets greater when approaching the anode and leads to an amplification of the original charge. This is called gas amplification. The measure of this is the gas-gain G_{gas} [7]. In order to achieve a high density of ionizations and low losses, the detector is filled with an nobel gas. To improve stability of the detector a quench gas such as CO_2 is added.

2.2.1 Gas Gain

The gas gain G_{gas} is an important characteristic of gas chamber detectors. It describes the ratio between the amount of initial electron inside the detector $N_0 = N(s_0)$ and the
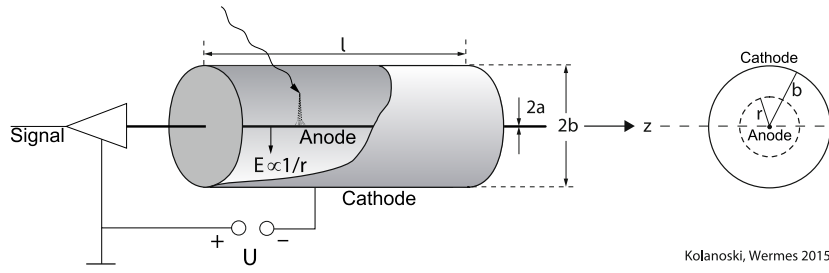
Figure 2.2: Schematic drawing of a counting tube showing the principle behind gas detectors. Shown is a cylindrical design with the anode wire in the middle and the cathode forming the outer shell. [7, p.182, fig. 7.4]

amount that reaches the anode $N(s_a)$. Assuming effects caused by recombination and electron attachment are negligible, it follows that [7, p. 190, eq. 7.11]:

$$G_{\text{gas}} := \frac{N(s_a)}{N_0} = \exp\left(\int_{s_0}^{s_a} \alpha(E(s))ds\right) \tag{2.1}$$

where $\alpha(E(s))$ is the amount of ions created per distance dependent on the electric field $E(s)$. Defining $n := \frac{W_{\text{ionisation}}}{\langle\epsilon\rangle} \cdot \frac{dN_0}{dt}$ as the mean rate of primary ionizations with $\langle\epsilon\rangle$ being the mean ionization energy and $W_{\text{ionisation}}$ being the work for ionization in the detector gas. It can be used that $q = N \cdot e$ and $I = \frac{dq}{dt} = \frac{dN}{dt} \cdot e$. Assuming that G_{gas} is constant in time this leads to:

$$
\begin{aligned}
I_{\text{anode}} &= \frac{d}{dt}q(t, s_a) \\
&= e \cdot \frac{d}{dt}N(t, s_a) \\
&= \frac{dN_0}{dt} \cdot G_{gas} \cdot e \\
&= \frac{\langle\epsilon\rangle}{W_{\text{ionisation}}} \cdot n \cdot G_{\text{gas}} \cdot e
\end{aligned} \tag{2.2}
$$

Since the anode current is proportional to the gas gain $I_{\text{anode}} \sim G_{\text{gas}}$, measuring it allows for observation of the relative change in gain, when assuming that the rate of primary ionization has not changed. As later discussed, this is the chosen method of determining the relative gain across the active area of the CBM TRD chambers.

2.2.2 Modes of Operation and Chamber Types

Gas detectors are used in a variety of different applications and therefore come in a variety of different designs. One of the distinctions is the operating voltage. It can be distinguished between different regions of operation, which are displayed in figure 2.3 . In the regions of
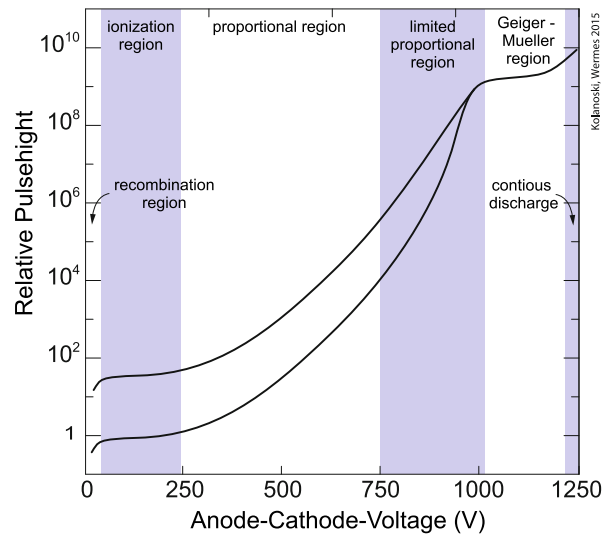
Figure 2.3: Regions of operation of a gas detector. Showing the region of recombination and ionization region, the proportional region, the limited proportional region, the geiger-mueller-region and the continues discharge. [7, p. 197, fig. 7.10]

recombination and ionization lower voltages lead to no amplification. In the proportional region, the signal is proportional to the initial charge. In the Geiger-Müller region saturation causes the signal to no longer be proportional to the initial charge. The limited proportional region is the transition between the proportional region and the Geiger-Müller Region.

Since the CBM TRD is a Multiwire Proportional Drift Chamber the following chapters will focus on this type of design. As the name suggests, this design lays within the proportional region, in which the amplified signal is proportional to the initial charge. Other designs include simpler counting tubes that do not offer any spatial resolution, such as Geiger-Müller-counters or proportional counting tubes. These types of detectors are often used to detect the presence or measure the intensity of radiation.

2.2.3 Multiwire Proportional Drift Chambers

Multiwire Proportional Chambers (MWPCs) commonly consist of a plane of anode wires between two cathode planes that are either flat sheets or wire planes themselves. This allows for a plane detector, while also offering the possibility of achieving spatial resolution. Particles can enter through an entrance window covering one face of the detector. To increase the thickness of the detector an additional drift area can be added between the entrance window and the cathode wire plane by applying an additional drift voltage between the cathodes and the entrance window. This creates a homogeneous electric field in the region, called drift region. This overall setup can be seen in figure 2.4. Due to the larger volume of the detector a higher detection efficiency can be expected for particles with mid to low absorption
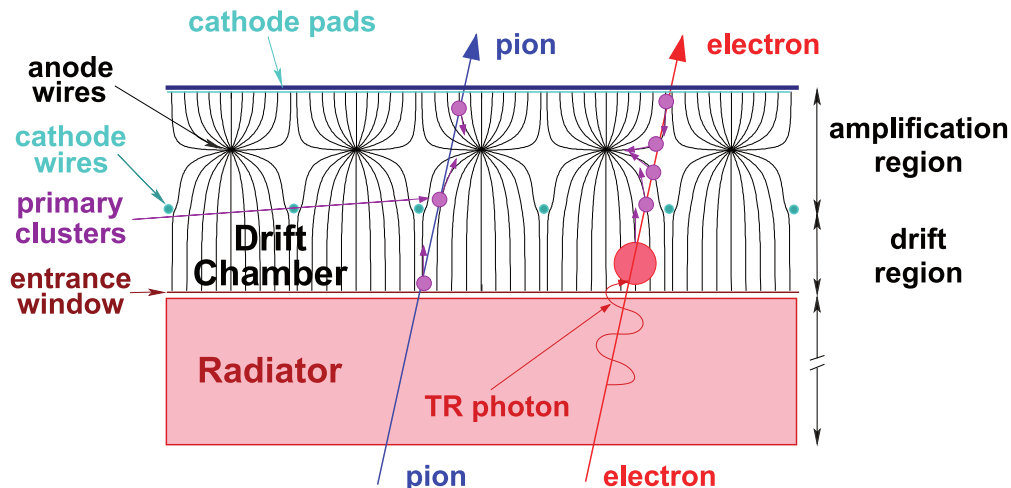
Figure 2.4: A cross-sectional view of a TRD showing both the radiator in front and the drift MWPC consisting of the drift and amplification regions. Entering from below are an electron and a pion, with the electron causing TR-photons in the radiator. Both then enter the drift and amplification region and cause primary clusters. [8, p. 35]

probability. The electric field in the drift region causes the electron to move into the area between cathode and anode wire planes, where gas amplification can happen. This region is therefore called the amplification region. Besides increasing the detector volume efficiency, measuring the drift time can give insight into the z-location of the initial ionization. In reality this is not done in the CBM TRD.

In order to achieve spatial resolution, it can be differentiated between two general approaches. Using the signal received by individual anode wires allows a resolution of $s/\sqrt{12}$ [7, p.220, eq. 7.45] along the orthogonal direction of the wires, with s being the wire distance. Alternatively the back cathode sheet can be split up into individual cathode pads allowing the signal to be read out at the cathode. This second approach is the one implemented in the CBM TRD.

2.3 Transition Radiation Detectors

Transition Radiation Detectors (TRDs) work by placing a radiator in front of a read-out chamber, which in the case of the CBM TRD is a MWPC. As shown in figure 2.4, an incoming particle will first pass through the radiator before entering the readout chamber. In doing so, electrons will cause the emission of a transition radiation (TR) at the boundaries of materials with different dielectric constants. Both the electron and the TR photons will then enter the MWPC, where they are detected. This allows for the distinctions between pions and electrons. The following thesis will focus on the MWPC, which will be tested without a radiator present.

2.4 CBM TRD
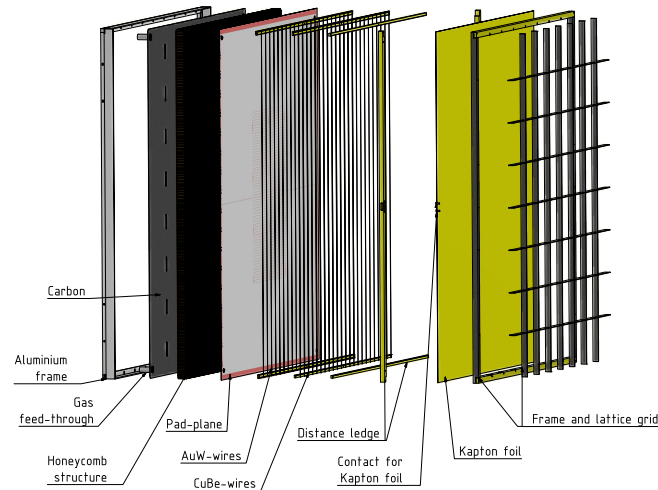
(a) Exploded-view of the different layers of the read-out
    chamber [8, p. 65, fig. 5.10]
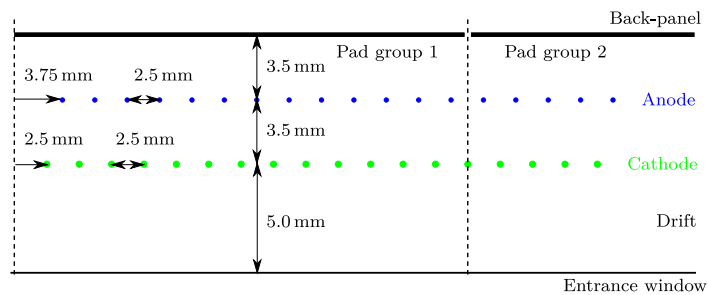
(b) Cross-sectional view of the TRDs active volume [8, p. 67,
    fig. 5.13]

Figure 2.5: An exploded and cross-sectional view of the TRD showing the different compo-
            nents of the TRD and showing the spacing of the wire planes.

The CBM TRD chambers are drift MWPCs behind a radiator, as described in section 2.3.
As shown in figure 2.5, the chambers consist of an entrance window made of kapton foil being
held in place by a carbon fiber lattice grid. As detailed in appendix A this grid has a depth of
15 mm and limits the deformation of the window caused by gas pressure inside the chamber
to below 1 mm [8]. Behind the entrance window is the drift region with a depth of 5 mm
deep. The amplification region is symmetrical with a 3.5 mm distance between the anode
wire plane and the pad-plane as well as 3.5 mm between the anode and cathode pad plane.

Both the anode and cathode wires are grouped up into 6 wire sections of equal size. When
mounting the chamber as described in chapter 3, the wires run horizontally with the sections
being numbered starting at the bottom with section 1. The individual sections can either
be directly connected to a power supply or wired in parallel. In the later case the circuit

connecting all sections lies on the filter-board, which is shown in figure 2.6. Optionally, capacitors can be installed on the filter board, but this is not done in this context.
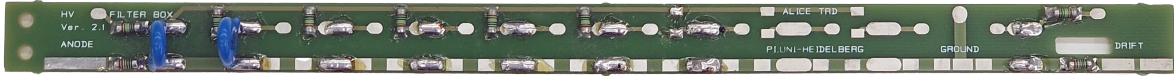
Figure 2.6: High voltage filter board supplying the entrance window and different wire sections with the incoming voltage.

The back panel consists of a pad plane that is connected to the front end electronics, which are then used for the read-out of the signal produced by the detector. Each TRD layer will be made out of 54 chambers, which are separated into 4 different types [8]. One additional type, type 8, is a prototype design which will not be used in the final experiment. Type 8 is used as a testing ground for all measurements carried out in this thesis. Each of these types differentiates itself by its size and the number of pads. The dimensions of both, the chambers themselves and the pads, can be found in appendix A. The development and production of these modules is being done in cooperation between the University of Münster, the University of Frankfurt and the University of Bucharest. As of the beginning of October 2023 the series production of the type 5 chambers being built in Münster and Frankfurt is ongoing with first chambers being finished.

2.5 Experimental Goals of this Thesis

For the purpose of quality assurance on newly produced chambers, it is useful to spatially map the gain across the chamber geometry and check for uniformity. This will ensure that the chamber was constructed as expected and may help identify issues in production. Since this should happen as early as possible in the process of construction, it is done before the installation of any front end electronics. Measuring the anode wire current is the most simple and direct approach to assess the gain, as described by equation (2.2). Readout of the cathode pads is therefor not neccecarry. The goal of this thesis is to perform test measurements on an already existing type 8 chamber built in 2016 and use these as a testing ground to develop and validate a process with which future chambers will be tested.

3 Experimental Setup

The gain measurement in this setup is realized without read-out electronics connected to the chamber, but based on the currents delivered to the wire electrodes, in accordance with equation (2.2). The spatial resolution that can be obtained from the current is restricted to the segments of the anode wire layer, described in section 2.4. In order to create a finer resolution, smaller chamber locations are addressed, by focusing a radioactive calibration source at known positions on the chamber while measuring the anode current.

The overall experiment can thus be split up into two main objectives, which the experimental setup tries to achieve:

1. Operating the chamber and measuring the anode current. This involves a gas supply and a high voltage power supply with either integrated or separate current readout. Since the anode current is expected to be on the order of a few nA, the current measurement needs to have similar precision.

2. Positioning of the radioactive source in front of the entrance window and moving it in repeatable way, in order to measure at different positions.

An overview of the general setup can be seen in figure 3.1 and builds on the work done by Johannes Beckhoff [9]. It consists of the chamber mounted to a CNC-Machine, described in section 3.4. Fitted on the tool head of the CNC-Machine is an ^{55}Fe X-Ray source, described in section 3.2. This allows the source to be positioned and moved in front of the chamber. The anode voltage is supplied by an ISEG *EHS F630p-F* power supply and the drift voltage is supplied by an ISEG *EHS 8630n-F* power supply (see section 3.3). The chamber is filled with *Sagox18*, which is fed into the chamber with a flow controller at a rate up to 5 l/h (see section 3.1).

In the following subchapters the separate elements of the setup and the program developed to make these elements work together are described.
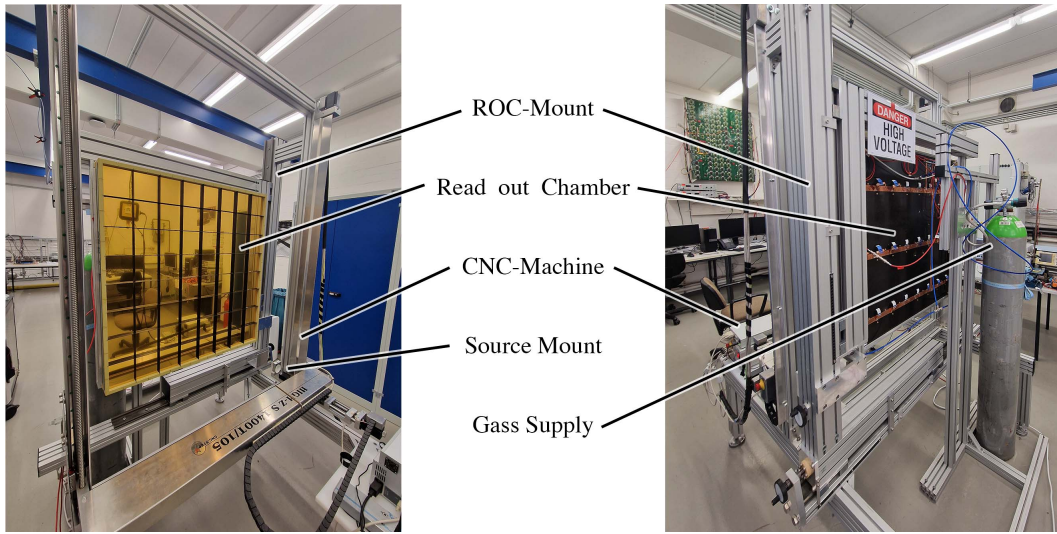
Figure 3.1: The overall gain measurement setup, shown from the front (left) and back (right), including the read-out chamber that is being tested, the chamber mount, the gas supply and the CNC-machine that holds the radioactive calibration source.

3.1 Gas Supply

As described in section 2.2 the chamber needs to be filled with a suitable gas mixture in order to allow for amplification of the incoming signal. In the final setup at the GSI the chamber will be filled with Xenon and CO_2. In these tests, since using Xenon would entail significant costs, the chamber is operated with *Sagox18*, an 82% Argon - 18% CO_2 mixture, commonly used in welding operations. The amount of gas entering the chamber is controlled with a low volume variable flow meter (*Kobold KFR-2112N0*) [10]. This flow meter it calibrated for air and allows the flow rate in air to be adjusted between $0.04\,l/min$ and $0.5\,l/min$ with a precision of $\pm 0.03\,l/min$. Since in this case, *Sagox* is the used gas, the indicated flow rate needs to be corrected. According to [11] this can be approximated by:

$$q_{Sagox} = \sqrt{\frac{\rho_{Air}}{\rho_{Sagox}}} \cdot q_{Air} \tag{3.1}$$

with q being the flow rate of the corresponding gas and ρ being the density of the gases. With $\rho_{air} = 1.208\,kg/m^3$ [12] and $\rho_{Sagox} = (0.82 \cdot 39.95\,u + 0.18 \cdot 44.01\,u)/22.4\,l/mol = 1.82\,kg/m^3$ [13] the read of values needs to be corrected by a factor of 0.81. This results in an overall flow rate between $(2 \pm 1)\,l/h$ and $(24 \pm 1)\,l/h$. In this set up, the flow rate is set at or below $(5 \pm 1)\,l/h$. During the measurement process the flow rate is set to $(5 \pm 1)\,l/h$, in between measurements it is set lower at $(2 \pm 1)\,l/h$ in order to avoid contamination of the chamber.
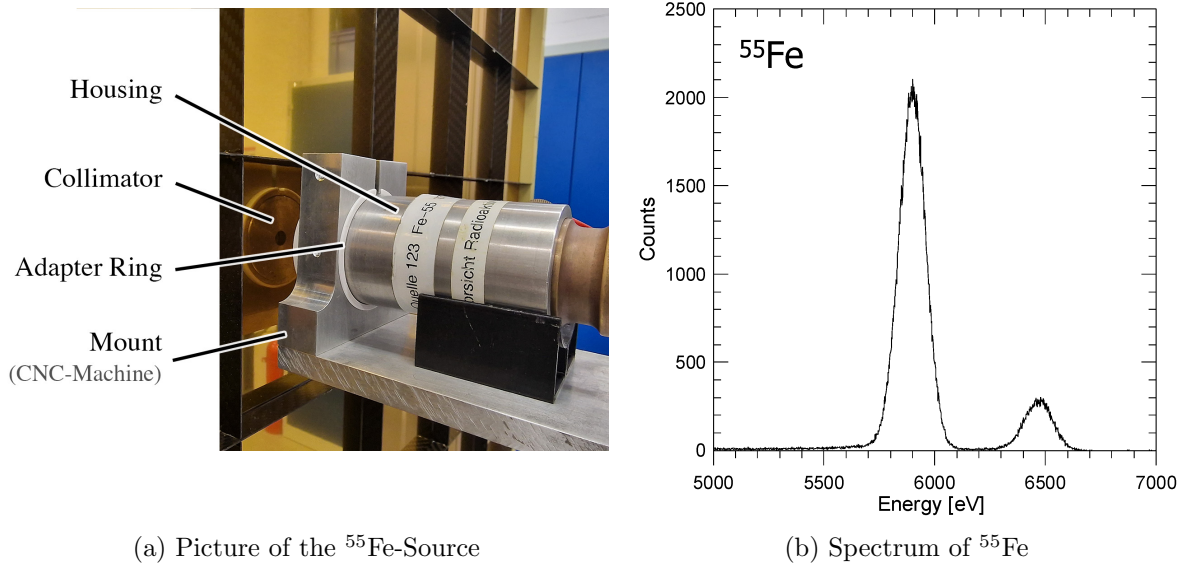
(a) Picture of the ^{55}Fe-Source

(b) Spectrum of ^{55}Fe

Figure 3.2: The ^{55}Fe-Source used as the calibration source, displayed in its mounting on the CNC-Machine and the spectrum of ^{55}Fe [14] with the K_α and K_β lines clearly visible.

3.2 Radioactive Calibration Source

The selected radioactive source is an Iron-55 (^{55}Fe) isotope probe that is placed in front of the chamber. ^{55}Fe is chosen due to photon emission with energies in the region of maximum absorption by the read-out chamber, which intern is also similar to the photons generated by the radiator that will be mounted in front of the chamber later on [8, p.80ff.]. ^{55}Fe decays via electron capture into Mn^{55}, with t$_{1/2}$ = 2.747 a [15]. The spectrum, shown in figure 3.2b, is characterized by the $K_{\alpha2}$ = 5.887 65 keV, $K_{\alpha1}$ = 5.898 75 keV and, K_β = 6.490 45 keV lines. The intensity of the source is, in accordance with equation (2.2), directly proportional to the anode current. A stronger source would therefore lead to a stronger signal received. The ^{55}Fe source used is displayed in its mount in figure 3.2a. It has an intensity of 37 Mbq measured in November 2015 which results in an intensity of 5.1 Mbq at the time of the experiment in September 2023. The source has a directional opening with a collimator being mounted in the front, which can be changed to allow different opening sizes. Smaller openings would increase spatial resolution of the measurements, since the width of the area illuminated by the source will decrease, but this would also decrease the amount of signal received. Therefore, all measurements are done with the largest available collimator, which has an opening with the radius $r_{col.}$ = 4 mm. The actual radioactive isotope is mounted 7.25 mm behind the front face of the collimator, with the collimator being 4.9 mm thick. This forms an illuminated region that can be described as a section of a sphere, later discussed in section 4.1.1.

3.3 HV-Source & Current Readout

The voltage supplied to the chamber anode is set between $1850\,\mathrm{V}$ and $2000\,\mathrm{V}$, while the drift voltage is set between $-100\,\mathrm{V}$ and $-500\,\mathrm{V}$. The specific voltages chosen are dependent on the condition of the used chamber and outside conditions. Higher applied voltages will lead to higher gain (see figure 2.3) but will increase both the leakage current and/or the risk of uncontrolled discharges, which will lead the voltage to shut down as a safety measure. The leakage current forms a baseline that is not constant over time and therefore introduces uncertainties further discussed in section 5.3.

The voltage on the anode side is supplied by an ISEG *EHS F630p-F* power supply, while the drift voltage is supplied by an ISEG *EHS 8630n-F*. Both power supplies allow for multichannel control of the voltage and readout of both the voltage and the current via Simple Network Management Protocol (SNMP) communication. This allows integration into the overall control program (see section 3.5). The multichannel capability of these devices would theoretically allow separate readout and control of the different wire segments. Although possible, this functionality is not further explored.

Both power supplies allow voltage settings with long term stability of $150\,\mathrm{mV}$, which is more than sufficient for these purposes. The current measurement has a relative uncertainty of 0.02% and a resolution of $6\,\mathrm{nA}$, given by the manufacturer [16].

The limitations of this method of current measurements are further explored in section 5.3.

3.4 CNC-Machine / XY-Motion-Table

In order to automate the positioning of the radioactive calibration source, a 3 Axis CNC-Machine, commonly called the XY-Motion-Table, is used. CNC-Machines (*Computer Numeric Control*) are commonly used in manufacturing and allow a tool head to be moved in three-dimensional space by digitally addressing actuators that control one respective axis each. Thus, mounting the calibration source to the tool head allows it to be moved by digitally addressing the machine. The CNC-machine used in this case is a *High-Z S1400T/105* build by the company *CNC-Step e.K.*. The specific model possesses a travel range of $1050\,\mathrm{mm}$ x $1400\,\mathrm{mm}$ x $110\,\mathrm{mm}$ and is thus large enough to test the whole active area of all currently planned CBM TRD chamber types. The precision of the positioning is given by the manufacturer as $0.01\,\mathrm{mm}$ [17]. The machine can be controlled with a *CNCCON*-controller [18] which serves as an interface between the machine and the computer, allowing for a serial connection to the computer running the control script, described in the following chapter.
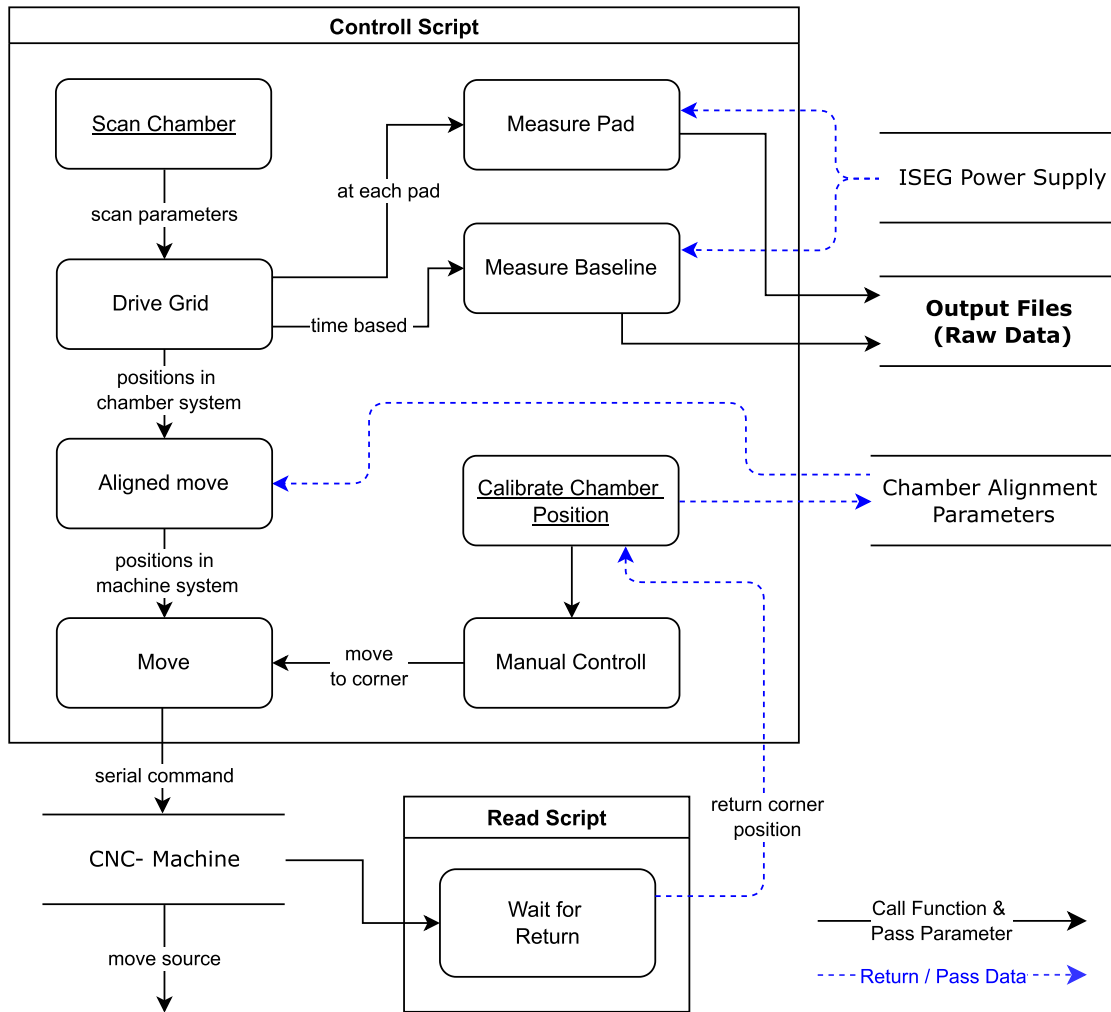
Figure 3.3: A flowchart showing the general logic of the python script controlling the CNC-Machine and measuring the current. Scanning a chamber is the central function of the script that generates the Output Files, which contain the raw data of the measurement results.

3.5 Source Positioning & Control Script

In order to create a spatially resolved gain map, the ^{55}Fe-source must be positioned in front of the chamber by the CNC-Machine and moved across the chamber geometry while gain measurements are taken at each position. The movements and measurements are controlled with a *Python* script, combining both the control of the machine and the readout from the power source. Building on the work done by Johannes Beckhoff [9], the CNC machine is controlled through the *Python* script via a serial connection. The overall program can be separated into 2 parts: Commands are sent with the help of the control script and returning messages are interpreted by the read script, which verifies that the command was executed. Communication between the two scripts is achieved with a socket connection. To achieve accurate timing of the current measurements, the readout from the power supply is included

in the control script. The current is read out via SNMP communication with the *ISEG* power supply (see section 3.3). A simplified version of the logic of the script can be found in figure 3.3.

The script, which is controlled by a terminal interface, is the main way, a process for future scans in the production of MWPCs for the CBM experiment has been implemented. It allows for automated measurements of spatially resolved gain maps and is available on GIT.

Besides controlling the CNC-machine and measuring the voltage and current, one of the program's main features is describing the position of the mounted chamber and the geometry of different chamber types (see appendix A), in order to accurately move the tool head to a position relative to the chamber. This positional calibration is described in the following chapter.

When scanning, the machine will drive in a grid pattern along the chamber, which can be seen in figure 3.4b, while measurements of the anode currents and voltages at each grid point are taken. In order to improve statistics, the chamber will be scanned multiple times, thereby taking measurements for each position at different points of time. Since the current baseline, further discussed in section 5.3, needs to be remeasured at given time intervals, the machine will periodically drive to a safe position, where the radiation source is shielded by an aluminum plate and measures the baseline.

3.5.1 Spatial Chamber Calibration

Since the source needs to be driven to a given position in front of the chamber, knowledge of the spatial position of the chamber is needed, in order to operate the machine. Special attention needs to be directed towards the z-axis (distance between chamber and source).

Generally, close distances between the source and the chamber are preferred, since this will concentrate the radiation on a smaller illuminated area of the chamber and therefore improves the sharpness of the scan, while also reducing the absorption of photons by the air. However, physical contact between the machine and the chamber would cause damage to the chamber and must be avoided. Therefore, the accuracy of the described chamber position is vital in ensuring that this does not occur, while also driving as close to the chamber as possible. In order to describe the chamber position, two coordinate systems, shown in figure 3.4a, are introduced:

The machine coordinate system   (machine system) simply describes the three axes in which the CNC machine moves. The origin is the home position of the machine in the bottom right
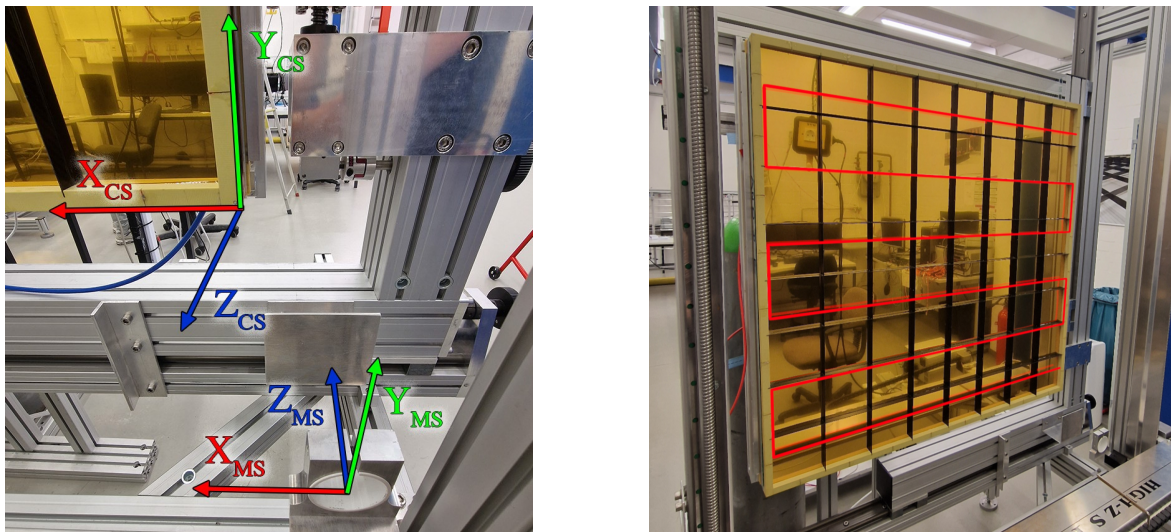
(a) Origins and base vectors of both the ma-
chine and chamber system shown in the
experimental setup.

(b) The path of the scan pattern the machine
follows when scanning a chamber along
the pad centers shown as a red line in front
of the chamber.

Figure 3.4

corner, which the machine uses to calibrate its position when initializing the machine after
startup, as shown in figure 3.4a.

The chamber coordinate system   (chamber system) describes the relative position to the
chamber. Its origin is defined as the bottom right corner of the chamber frame, as shown in
figure 3.5a. The x- and y-axis run along the frame of the chamber and are therefore span-
ning a surface that describes the position of the chamber. Since the source is pointed in the
direction of the machine's z-axis, the z-axis in the chamber system is chosen to be identical
to the machine system's z-axis. This ensures that moving the z-position of the source in the
chamber system will not change the center of the illuminated area on the chamber.

The goal of determining the relative position of the chamber can now be seen as being
equivalent to finding a transformation between the chamber system and the machine system.
In order to determine this transformation, the position of given points on the chamber in the
machine system is measured. Since the CNC-Machine already records its current position
with a precision of 0.01 mm (see section 3.4) using the tool head as a measuring device is a
simple and effective method to do so. Since contacting the chamber with the machine is not
an option the tool head is aligned with a given point in x- and y-direction, while a small gap
is left between the chamber and the machine in the z-direction. The size of this gab is then
measured with calibers.
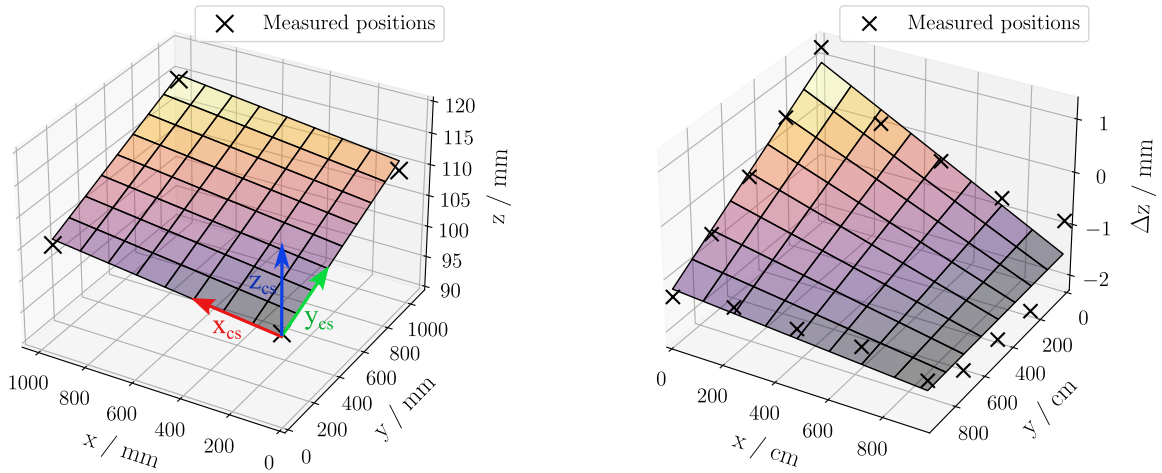
(a) The plane describing the chamber's position in the machine system in accordance with equation (B.1). The chamber system's origin and basis vectors are visible at the bottom right corner.

(b) The difference in z-position between the planar calibration and a further z-correction. Displayed in the chamber system of the planar calibration $\vec{r}_{pc}$.

Figure 3.5: Shown above are both planar and z-corrected calibrations, resulting from the measured points, shown in the figures, fitted against the functions of the plane calibration and z-correction. The resulting parameters are shown in appendix D.

Plane calibration   - The plane calibration assumes that the chamber is a flat plane, the transformation from the chamber system to the machine system can be described by translation and rotation, described by a (3×3) matrix T_{pc}. With:

$$\vec{r}_{pc} = T_{pc} \cdot \begin{pmatrix} x_{cs} \\ y_{cs} \\ 1 \end{pmatrix} - \begin{pmatrix} 0 \\ 0 \\ z_{cs} \end{pmatrix} \tag{3.2}$$

$\vec{r}_{cs} = (x_{cs}, y_{cs}, z_{cs})^T$ being a point coordinate in the chamber system and $\vec{r}_{pc}$ being the point in the machine system based on the transformation or the plane calibration. The derivation of this equation can be found in appendix B. In order to calculate this matrix, the position of all four corners of the chamber inside the machine system are measured. From the chamber geometry, the corner positions in the chamber system are already known. The least squares solution for the transformation between the points in the chamber and machine system is found using *numpys* linear algebra package [19]. An example of this correction can be seen in figure 3.5a.

Z-Correction   - In order to increase the precision of the description of the chamber in the z-direction, the z-position of the chamber frame is measured along 16 positions on the frame

of the chamber. This is necessary since initial tests showed deviation from the planar fit, visible in figure 3.5b.

The description of the x- and y-positions of the chamber remain identical to the previous planar description. For the z-direction, the 16 measured positions are fitted against the following function, using scipy's *curve fit* function [20]:

$$
\vec{r}_{zc} = \begin{pmatrix} 1 & 0 & 0 & 0 \\ 0 & 1 & 0 & 0 \\ p_1 & p_2 & p_3 & p_4 - z_{cs} \end{pmatrix} \cdot \begin{pmatrix} x_{pc} \\ y_{pc} \\ x_{pc} \cdot y_{pc} \\ 1 \end{pmatrix} \tag{3.3}
$$

With p_n being the fit parameters, x_{pc} and y_{pc} being the coordinates stemming from the planar correction, z_{cs} being the z-position in the chamber system and $\vec{r}_{zc}$ being the coordinate of the point in the machine system after applying the Z-correction. The derivation of this function can be found in appendix C and an example of the results of this correction can be found in figure 3.5b.

This further z-correction allows the CNC-machine to keep a constant distance to the surface described by the chamber frame, which is assumed to be the parallel to the wire plane. It is unclear why this non-planar behavior of the chamber is observed. Future chambers might not need this additional correction, but for all scans done in this context this type of spatial calibration was used.

A further correction could be implemented, describing the deformation of the entrance window due to pressure inside the chamber, further reducing the distance between the ^{55}Fe-source and the chamber.

4 Approximation of expected external Effects

It is expected that scans will show some effects caused not by a change in the gain but by a change in the rate of primary ionizations. The first of these effects is caused by the carbon grid in front of the chamber, displayed in figure 2.5a. When part of the illuminated area of the ^{55}Fe source hits the carbon grid some photons are absorbed, reducing the amount that reaches the detector.

The second effect is expected towards the edges of the chamber and results from the fact that the illuminated area of the ^{55}Fe will partially miss the active area of the detector.

The third of these effects is caused by the deformation of the entrance window caused by the gas pressure inside the chamber, as described in [21]. This increases the chamber volume and lowers the distance between the ^{55}Fe-Source and the entrance window, therefore also increasing the rate of primary ionization, towards the center of the chamber.

The following chapter will attempt to approximate the theoretical extent of the mentioned effects. Since this is only an approximation, any uncertainty considerations are omitted here.

4.1 Effects caused by the Carbon Grid and Chamber Edges

The effect of the carbon grid on the gain measurement is approximated with an algorithm, in which the ^{55}Fe-source is assumed to be a point source that casts a large number of photons at the chamber geometry. Vectors go out from the source in specific directions (φ, θ) and can be seen as an emission of photons with the intensity I in that specific direction, that causes a certain amount of primary ionizations n_{ray} inside the chamber. The overall rate of primary ionizations in the chamber n is the sum over all vectors cast by the point source in the illuminated region. In accordance with equation (2.2) n is proportional to the measured current. Therefore, calculating n for different positions of the ^{55}Fe source and examining the relative change will give insight into the expected relative change of the observed current.

For each photon, three values are calculated: the distance s_{air} the ray travels through the air, the distance s_{cf} the ray travels through the carbon fiber of the grid and s_{ch}, which is the

distance of the intersection between the ray and the active chamber volume. It is assumed that n_{ray} is dependent on s_{ch}, while s_{air} and s_{cf} cause a reduction in intensity of the ray, before entering the chamber. Overall, the amount of primary ionizations by a single ray in each time interval can be described as being proportional to [6]:

$$n_{ray(r,\varphi,\theta)} \sim I_0(\varphi) \cdot (1 - e^{\mu_{Ag} \cdot s_{ch}}) \cdot e^{\mu_C \cdot s_{cf}} \cdot e^{\mu_{air} \cdot s_{air}}. \tag{4.1}$$

The distances are derived based on the chamber geometry (described in appendix A), the position of the source and the angle, with which the ray is cast from the source. Since this geometry includes the edges of the chamber, the calculation will also show the effect of rays going past the chamber, when the source is close to an edge. μ_{Ag}, μ_{C} and μ_{air} are the linear attenuation coefficients, according to [6]. The carbon fiber of the lattice grid is approximated assuming it is made out of pure carbon and using the density of carbon fiber in accordance with [22]. The resulting factors can be found in table 4.1.

Each ray also takes into account the radial intensity $I_0(\varphi)$ of the source for a given angle, as described in the following chapter. The results of this overall approximation, together with actual measurement results, can be found in section 6.2.

Table 4.1: Mass attenuation coefficients μ/ρ, densities ρ and resulting linear attenuation coefficient μ of air, argon and carbon fiber. [6] & [22]

	μ/ρ [cm^2/g]	ρ [g/cm^3]	μ [cm^{-1}]
air	23.41	1.205×10^{-3}	2.82×10^{-2}
argon	259.3	1.622×10^{-3}	4.21×10^{-1}
carbon (fiber)	10.95	1.8	19.71

4.1.1 Approximation of the Iron-55 Source Intensity

$I_0(\varphi)$ is introduced as the angle based intensity of the source. This intensity is approximated by assuming that the hole in the collimator in front of the source and the radioactive isotope located behind the collimator form a cylinder with the radius $r_{col.}$ and depth $d_{col.}$. The intensity is then assumed to be the area of the bottom of the cylinder that is visible when looking through the top of the cylinder at the angle φ, which could also be seen as the area of the source visible when looking through the front of the collimator. This principle is shown in figure 4.1a. The position of the point source is in the center of the collimator. Therefore, the z position of the point source given by $z = d + d_{col.}/2$ with d being the distance between the front of the source and the carbon grid. Adjusting the equation for the intersections of two circles [23], in order to get the area of the bottom of the cylinder visible at the angle, φ gives (this derivation can be found in Appendix E):
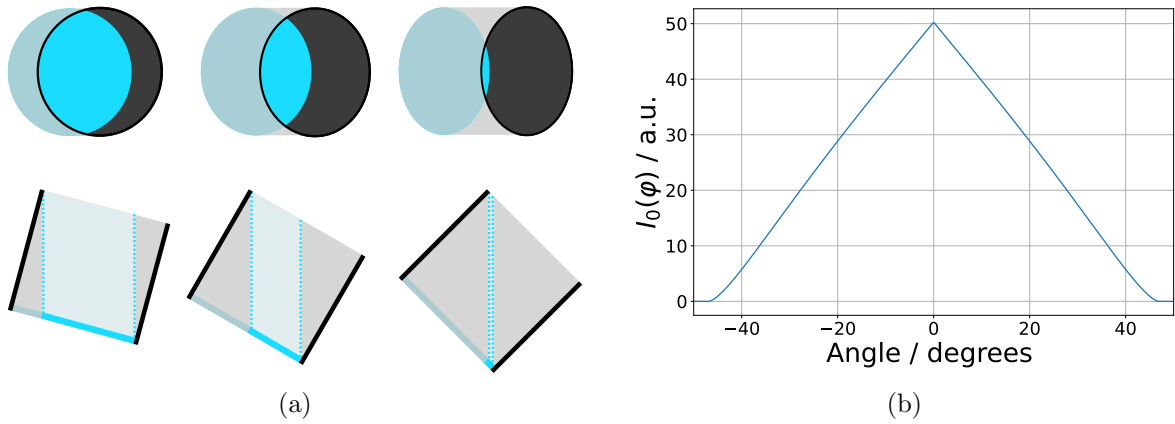
Figure 4.1: (a) shows the principle behind calculating the intensity of Fe^{55} source at a given angle, by assuming that this intensity is proportional to the area of the bottom of a cylinder representing the hole inside the collimator of the source. (b) shows the resulting intensity at different angles φ using equation (4.2) with $r_{col.} = 4\,\text{mm}$ and $d_{col.} = 7.25\,\text{mm}$.

$$I_0(\varphi) = 2r_{\text{col}}^2 \cdot \cos^{-1}\left(\frac{d_{\text{col}}}{2r_{\text{col}}} \cdot |\tan(\varphi)|\right) - \frac{1}{2} \cdot d_{\text{col}} \cdot |\tan(\varphi)| \cdot \sqrt{4r_{\text{col}}^2 - (d_{\text{col}} \cdot \tan(\varphi))^2} \quad (4.2)$$

Note that this function is not normalized, since only relative intensities are of relevance in this case. Furthermore, this function is only an approximation that tries to reduce the source to a point source, when in fact the collimator radius of $r_{col.} = 4\,\text{mm}$ is of considerable size compared to the lattice width of only $0.8\,\text{mm}$ [8, p. 67]. A more realistic simulation without this approximation, that also includes uncertainty considerations could therefore be sensible and would be needed in order to correct for the effects caused by the carbon grid. Drawing the function for the given ^{55}Fe source with $r_{col.} = 4\,\text{mm}$, $d_{col.} = 7.25\,\text{mm}$ results in figure 4.1b. It can be seen the source has an overall opening angle of $\pm 46.7°$ with the maximum being at $0°$.

4.2 Effect due to Entrance Window Curvature

Since the read-out chamber is operated with an overpressure inside, the entrance window is curved outwards. This was measured and described in more detail in [21]. Therefore, the drift region will have a slightly larger volume in the center of the chamber causing the gas to absorb more ionizing radiation, leading to a higher measured current. Furthermore, the distance between the entrance window and the chamber will be smaller, leading to a reduction of the air between the chamber and the photon source. As an approximation, it is assumed that the entrance window is flat along the area, that is displaced by a distance of Δd towards
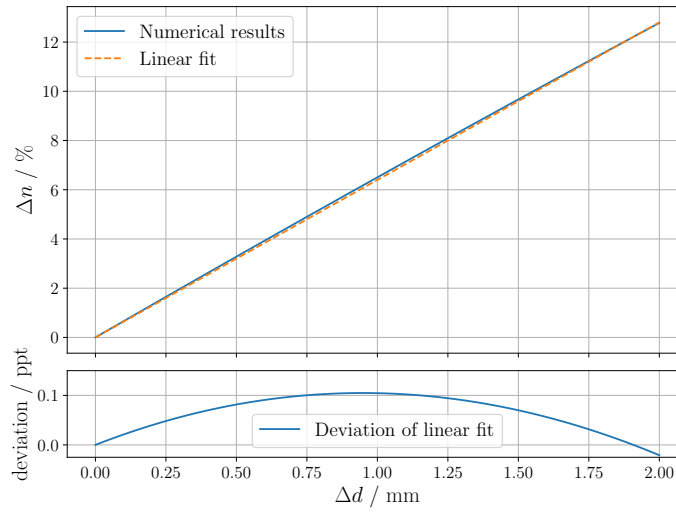
Figure 4.2: Approximation of the effect on the rate of primary ionizations and therefore the anode current caused by displacing the entrance window by a distance Δd in accordance with figure 2.5 and fitted with $\Delta n = 0.064 \cdot \Delta d$. The deviation between the fit and the actual data is shown below as beeing $\lesssim 0.1\,\text{ppt}$.

the source. For a photon hitting the chamber at the angle, φ amount of primary ionizations is calculated, analog to section 4.1:

$$n_{ray}(\varphi, \Delta d) = I_0(\varphi) \cdot e^{\mu_{air} \cdot (15\,\text{mm} + d_0 - \Delta d) \cdot \cos\varphi} \cdot \left(1 - e^{\mu_{Ag} \cdot (12\,\text{mm} + \Delta d) \cdot \cos\varphi}\right) \tag{4.3}$$

The relative change in amount of primary ionizations across the entire chamber and therefore also the relative change in current can then be calculated as:

$$\Delta n(\Delta d) = \frac{\int \cos(\varphi) \cdot n_{ray}(\varphi, \Delta d) d\varphi}{\int \cos(\varphi) \cdot n_{ray}(\varphi, 0) d\varphi} - 1 \tag{4.4}$$

Solving this integral numerically results in figure 4.2. The resulting function can be approximated linearly with a deviation to the numerical results below $\lesssim 1\,\text{ppm}$ in the range $0\,\text{mm} \leq \Delta n \leq 2\,\text{mm}$:

$$\Delta n = 0.064 \cdot \Delta d. \tag{4.5}$$

A further consideration is the change in the electric drift field due to the deformation of the entrance window. This leads to a real change in gain and therefor shouldn't be corrected for in this context. Simulations of this effect can be found in [8, p. 72: 5.4.3 Electrostatic calculations]. Results from a Garfield simulations assuming a chamber operated at $1850V/-500V$ filled with Xe/CO_2 $(85:15)$, show a change in gain of $\sim -6\,\%$ gain per $1\,\text{mm}$ deformation of the entrance window. At these operating parameters, the change in gain would therefor nearly cancel out with the change in rate of primary ionizations.

5 Methods

5.1 Measurement Parameters

All the following measurements were done on already existing type 8 chambers, build in 2016 [24]. Although this type of chamber is not foreseen to be used in the final CBM TRD setup at GSI, they serve as a good testing ground, while the production of type 5 chambers ramps up.

The distance between the front face of the source and the carbon grid was chosen to be $d = (2.5 \pm 0.4)\,\text{mm}$. This safety margin ensures that, even with the chamber being deformed by the gas pressure, no physical contact is possible. Including the depth of the lattice grid, the distance to the entrance window is $(17.5 \pm 0.4)\,\text{mm}$, when assuming that the entrance window does not deform. Based on the geometric considerations done in section 4.1.1, this results in an illuminated area with a width of $(31 \pm 1)\,\text{mm}$. With a triangular distribution, for any point of primary ionizations this results in an uncertainty off $(6.3 \pm 0.2)\,\text{mm}$, which is just below the pad width of the scanned type 8 chamber. Additionally, along the x-axis the delay in the current readout discussed in section 5.3.2 needs to be taken into account, which is detailed in appendix G. Since the following plots show the x- and y-position of the source against the measured current, this uncertainty is not displayed in the following figures, but should be kept in mind.

The chosen voltage will change both the baseline and the amount of gain inside the chamber. For all measurements, if not indicated otherwise, the anode voltage is set at $1990\,\text{V}$ and the drift voltage is set at $-400\,\text{V}$. This causes the baseline of the anode currents to be between $300\,\text{nA}$ and $400\,\text{nA}$, depending on environmental factors. This is not optimal, especially since the origin of the leakage current causing this baseline isn't fully understood, and the leakage current tend to show some hysteresis behavior, which is not explored further here, but could be relevant enough to justify more detailed measurements in the future. Since having baseline currents that are too low might cause issues with the current readout, a higher baseline can be beneficial. Furthermore, the decision was made to prioritize the amount of gain over the

baseline. It can be seen in figure 6.8, this higher voltage does in fact lead to a better signal-to-noise ratio. A higher voltage was not viable since it would cause uncontrolled discharges, leading the chamber to shut down.

Section 3 of the anode wires is disconnected from the applied voltage, since it showed excessive leakage currents starting at $1650\,\text{V}$ anode voltage, not allowing the chamber to reach the operating voltage. The anode wires were initially left floating, not connected to ground.

Since the baseline changes over time, regular baseline measurements are taken by measuring 20 data points every $180\,\text{s}$ in a secure position, where radiation can not reach the chamber. A smaller interval would likely lead to less uncertainty in the current measurement, but would also increase the time needed for scans.

The chamber position was calibrated as described in section 3.5.1 and the resulting parameters can be seen in appendix D, which also corresponds with figure 3.5.

If not stated otherwise, after reaching a position, the control-script waits $2\,\text{s}$ before measuring the voltage and current. This behavior is further discussed in section 5.3.2.

Any scan will always be a tradeoff between the precision and accuracy and the time needed to execute the scan. Therefore, rougher step sizes, reduced scan areas or smaller statistics are sometimes chosen. As discussed later in chapter 7, additional steps could be taken to improve the scan times or the scan quality.

5.2 Data Processing

The data produced by the control script (see section 3.5) consists of the voltage and current measured at every position throughout multiple scan cycles. All measurements are saved together with the position of the source, a unique ID for this position and the time of measurement. In addition, baseline measurements are taken at regular intervals by measuring 20 data points every $180\,\text{s}$. As an example plotting this raw data for scan 1 against time results in figure 5.1a. It can be seen that the baseline changes over time with the actual data points laying somewhere above the baseline. The difference between this baseline and the data point is the actual current caused by gas amplification in accordance with equation (2.2). In order to subtract the baseline from each data point, the baseline at the time of measurement is approximated by interpolating linearly between the average of the 20 data points taken at each interval of the baseline measurement. This forms a continuous baseline, which can be seen in figure 5.1b. It can then be subtracted from the currents measured at every position. The subtracted values taken over time are displayed in figure 5.1c. A fine oscillating peak structure can be observed. This structure is caused by the scan pattern being repeated over
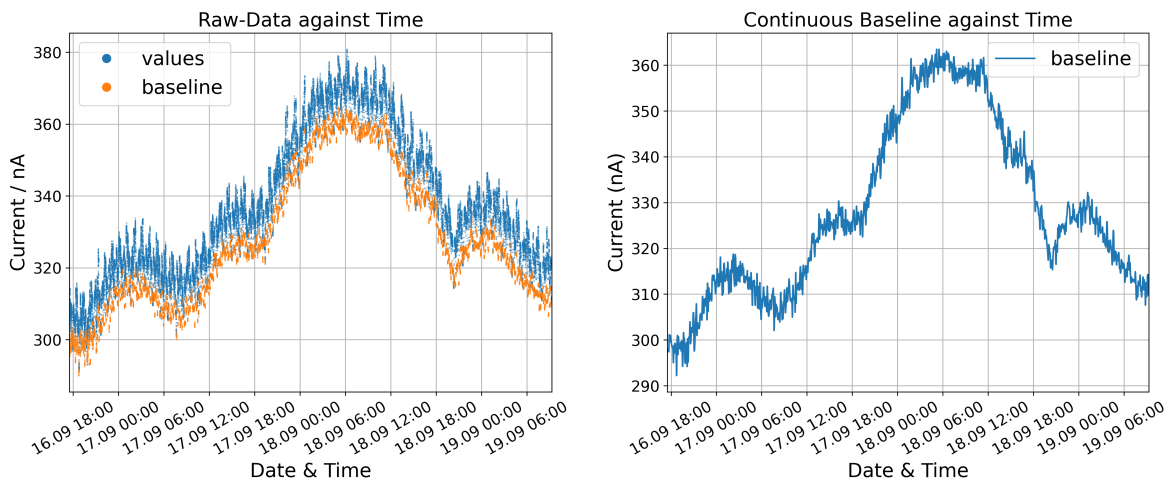
(a) Measured currents for positions in front of the chamber and for the baseline over time

(b) Linear interpolation off the baseline over time
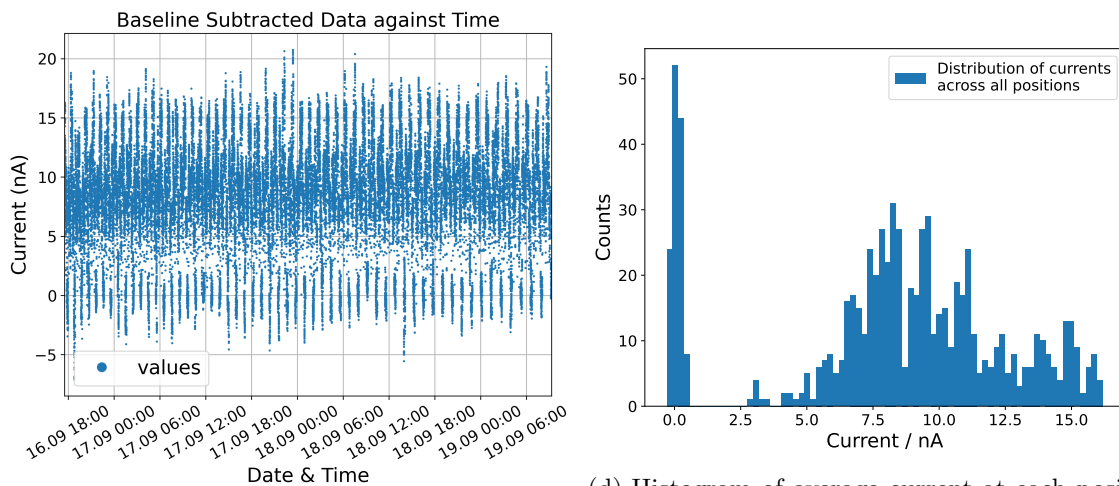
(c) Baseline subtracted values over time

(d) Histogram of average current at each position

Figure 5.1: Four plots showing the different steps of processing the data produced by scanning a chamber, using scan 1 shown in figure 6.1 as an example.

time. The machine therefore moves across the same positions in the same order. Regions of higher gain therefore cause repeating maxima every time they are scanned and regions of lower gain cause repeating minima every time they are scanned. The subtracted values are matched to each position based on the positions ID's. For every position, the average and standard deviations over all measurements, taken over different cycles, are calculated. A resulting distribution of the resulting averages for all pads can be seen in figure 5.1d.

Since the chamber is scanned multiple times measuring multiple data points for each position at different points in time, the uncertainty resulting from the interpolation of the baseline will be captured in the statistical uncertainty of the measurement series. This is opposed to the approach of, scanning the chamber once while taking multiple measurements at each

position, which leads to all measurement points for a position being consecutively measured. Thus, not accurately describing this uncertainty and leading to excessive noise in the gain map.

5.3 Baseline and Effects caused by the Current Readout

5.3.1 Baseline Measurements
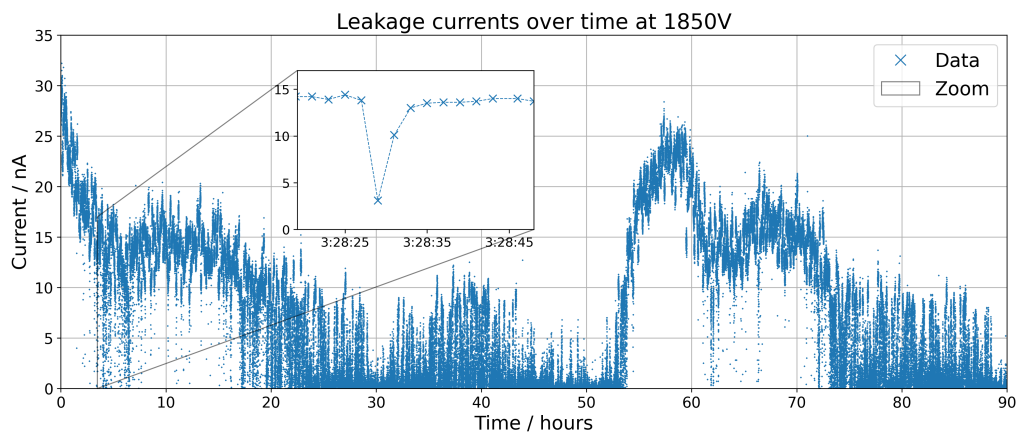
(a)
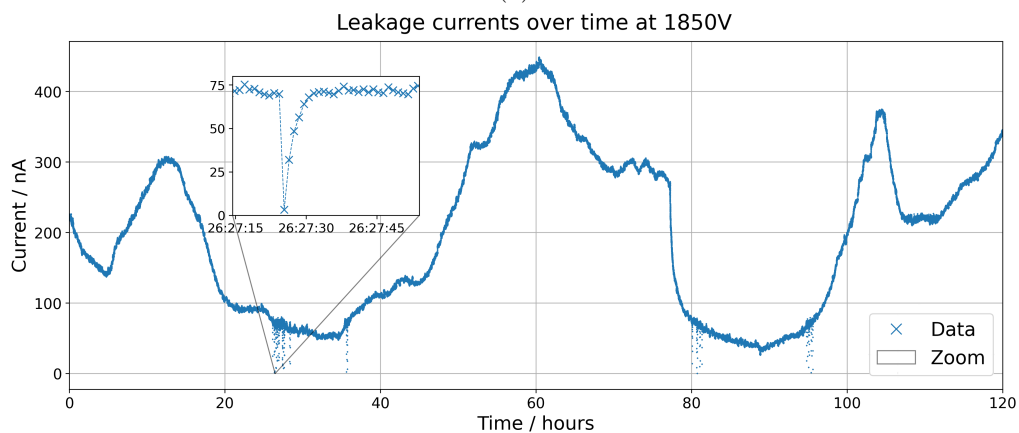
(b)

Figure 5.2: Measurements of the leakage currents over multiple days, measured at an 1 s intervals. Both measurements are performed with a filter board that was later replaced and a chamber, different to the one what was used in the scans. Both scans are performed at 1850 V without drift voltage applied and show different currents in different regions due to environmental factors during the measurements and/or recalibration of the ISEG Power supply. Highlighted areas show exemplary dropoffs in current.

For each current measurement, the baseline needs to be subtracted. This baseline is formed by the leakage current which is present without the ^{55}Fe source illuminating the active area of

the chamber. Since this dark current deviates over time with outside factors like temperature and humidity, the current needs to be remeasured during the course of a scan.

Two measurements of the leakage current were performed over multiple days with data points taken every $1\,\mathrm{s}$, to study the behavior of the baseline.

These measurements were taken with a different type 8 chamber than used for later scans. Further examination of the used filter board showed that the large baseline currents observed here were likely due to a defect on the filter board, which was later replaced. Therefore, the overall amount of leakage current and the susceptibility to environmental influences might be reduced in later and future scans, especially for newly built chambers. Nonetheless, the effects attributed to the readout method will be present in any measurement.

Figure 5.2 shows the measured baseline over the two measurement durations. It can be seen that both measurements show currents in different nA regions. This can be explained by environmental factors and the fact that between the measurements the *ISEG* power supply was recalibrated.

It is noticeable, that in some cases the voltage suddenly drops close to $0\,\mathrm{nA}$ and then recovers over a few seconds. This behavior can predominantly be seen in figure 5.2a but also occurs in figure 5.2b. This is assumed to be an artifact resulting from the way the current is read out and not part of the real data.

Figure 5.3 shows the change in current between consecutive measurement points for both measurement lines, with $\Delta I(t) = I(t + 1\,\mathrm{s}) - I(t)$. As expected, a distribution around $\Delta I = 0\,\mathrm{nA}$ can be seen indicating the current changing due to noise. Beyond that, figure 5.3a shows a band forming above $\Delta I = -I$, starting at $0\,\mathrm{nA}$ and going to between $I = 15\,\mathrm{nA}$ and $I = 20\,\mathrm{nA}$. This band corresponds with the dropoffs seen in figure 5.2a. The clean cutoff at $\Delta I = -I$ can be explained by the fact that the lowest possible value read by the ISEG power supply is $0.0\,\mathrm{nA}$. The fact that the band lays above this line is likely caused by the sampling rate not always capturing the lowest value. The recovery after the initial dropoff can also be seen as an increase of the values that lie around $0\,\mathrm{nA}$.

Figure 5.2a and figure 5.3b show similar dropoffs occurring between $65\,\mathrm{nA}$ and $75\,\mathrm{nA}$. Since in this case the initial current is significantly higher, the recovery takes longer and forms a band between $I = 0\,\mathrm{nA}$ and $I = 70\,\mathrm{nA}$ above the regular data in figure 5.3b. These dropoffs are also assumed to be an artifact connected to the readout method. Furthermore, figure 5.3b shows repeating areas of increased noise between $60\,\mathrm{nA}$ and $80\,\mathrm{nA}$, $210\,\mathrm{nA}$ and $230\,\mathrm{nA}$ and $360\,\mathrm{nA}$ and $380\,\mathrm{nA}$. The cause of this is not understood, but is likely also an effect caused by the ISEG device.
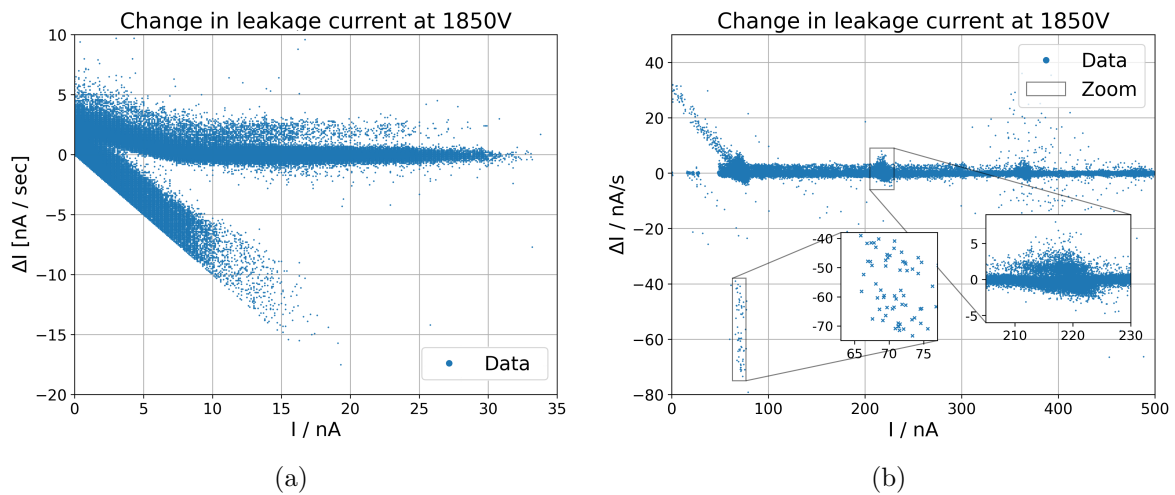
Figure 5.3: Difference in currents between consecutive $\Delta I(t) = I(t + 1\,\text{s}) - I(t)$ against the current at the start of the interval $I(t)$. Resulting from the measurements shown in figure 5.2, taken at 1 s intervals over multiple days, using a filter board and chamber that is not used in the following gain scans.

Due to these artifacts, measuring data with a baseline under 20 nA becomes increasingly difficult, since the drop-offs become more and more likely, eventually making it impossible to measure any real data. Most of the following scans were performed with significantly higher baselines avoiding the issues of the dropoffs. For any baseline intervals in which data points below 10 nA were measured all data from the interval is rejected. Since newly built chambers hopefully will not show the same level of leakage currents, as in the current setup, this issue might make scanning these chambers difficult. An improved current resolution, especially at low currents might therefore be needed.

Besides these observations, the need for remeasuring the baseline over time becomes clearly visible. For the following scans baseline measurements at 180 s intervals with 20 measurements points each were chosen. A more detailed analysis of the baseline characteristics could reveal an optimal interval striking a balance between the time increase needed to do the baseline measurements and the possibility of collecting more data points in the same time.

5.3.2 Delay in Current Measurements

A further artifact caused by the current readout is a delay in the current measurements. To measure this delay, the source is moved 10 cm away from the chamber along the z-direction, where it remains for 20 s, then moving 10 cm back to its initial position, also remaining there for 20 s. This sequence is repeated 100 times, while measuring current and voltage.

For each move, the average current over the 10 s before the start of the move is taken and used as the baseline, therefore accounting for the change in current over longer time periods.
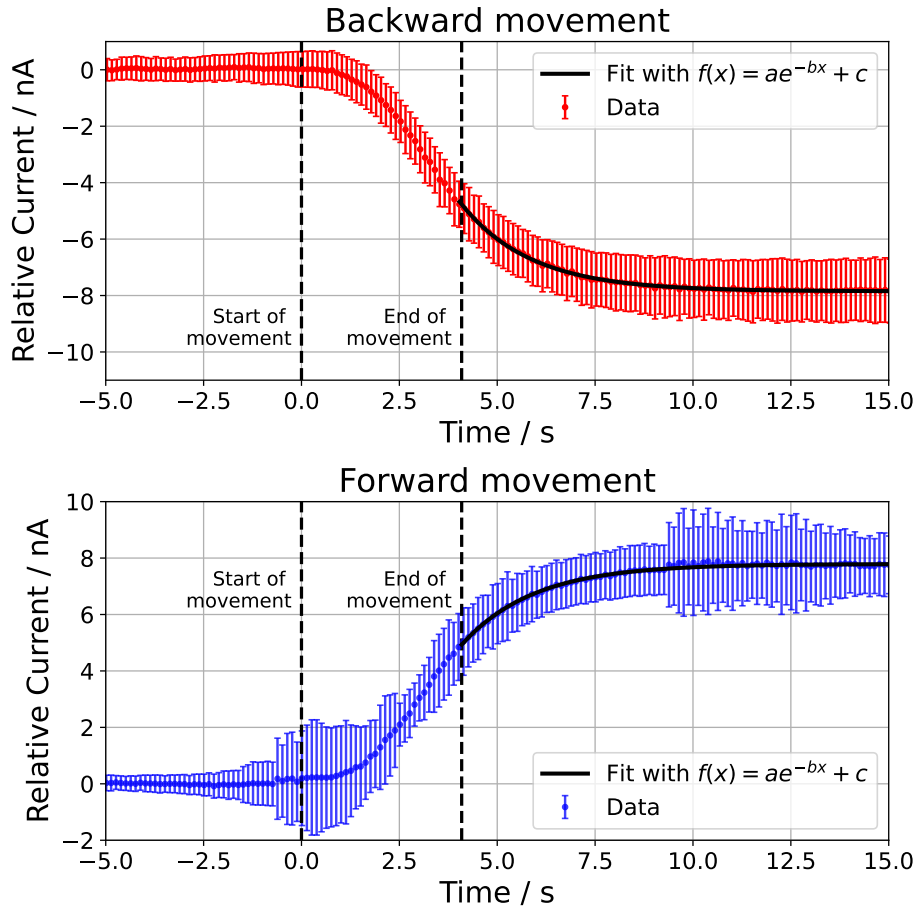
Figure 5.4: Current measurements taken while moving the source 10 cm forwards and backwards along the z-direction in front of the chamber and waiting 20 s at each position. The top shows the change in current while moving away from the chamber. The bottom shows the change in current while moving towards the chamber. A change in current after the end of a move can be observed in both cases.

Averaging the relative change in current during and after the move over the 100 cycles results in figure 5.4.

It can be seen that after finishing a move, the current changes for several further seconds and falls off towards its final value. Since it describes the data well, a fit against an exponential function is performed.

Using the least squares method with scipy's curve fit function [20] results in: $f_{for}(t) = (-26 \pm 4)\,\text{nA} \cdot e^{-(0.54 \pm 0.03)\,\text{s}^{-1} \cdot t} + (7.79 \pm 0.02)\,\text{nA}$ and $f_{back} = (30 \pm 4)\,\text{nA} \cdot e^{-(0.56 \pm 0.03)\,\text{s}^{-1} \cdot t} - (7.85 \pm 0.02)\,\text{nA}$. The falloff can thus be described with, $t_{1/2} = (1.23 \pm 0.07)\,\text{s}$ for reduction in current and $t_{1/2} = (1.28 \pm 0.07)\,\text{s}$ for increase in gain (see appendix G).

Although the cause of this effect is not understood, it is likely part of the current readout and is not a real effect of the chamber. In practical terms a higher delay between moving to
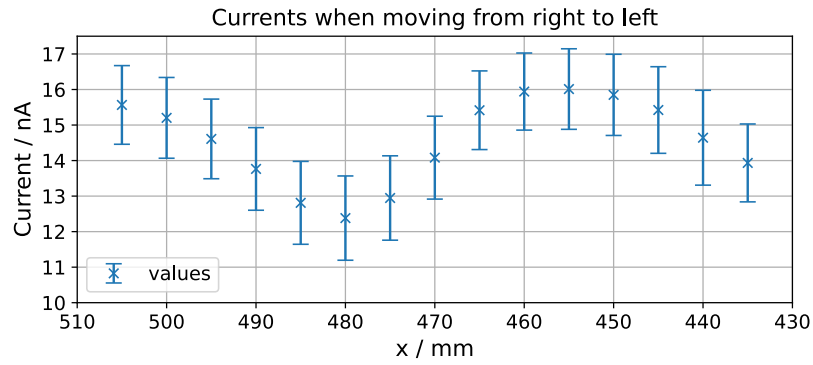
(a) Moving right to left
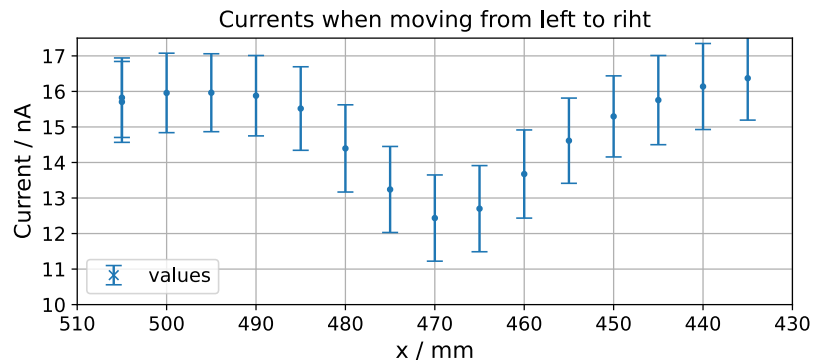
(b) Moving left to right

Figure 5.5: Current measurement at $5\,\text{mm}$ intervals in the x direction at $y = 7.25\,\text{mm}$ measured by moving the source from left to right (b) and right to left (a), while having no delay between movements and measurements.

a position and measuring the current will increase the sharpness of the produced scan in the drive direction but intern will also increase the time needed for measurements significantly. For all other scans, a delay of 2 seconds was chosen as a balance between reducing the influence of this effect and achieving reasonable scan times

Furthermore, it would be sensible to implement a feature that reverses the scan direction on every second measurement cycle. This would therefore not lead to an offset of the measured features due to the delay. This implementation is still outstanding and has not been realized in any measurements in this thesis.

To show the potential effects on a scan, a current scan is performed, in which the machine drives to the same positions along a line in the x-axis, once moving left to right and right to left, resulting in figure 5.5. To increase the visibility of the effect, the times between each move and the current measurement is set to $0\,\text{s}$. For later scans the delay is set at $2\,\text{s}$.

A reduction due to the carbon grid can be seen in both directions. The actual position of the lattice is at $x = 475\,\text{mm}$. The position of the minimum in the scan when moving right

to left is at $x = 480\,\text{mm}$ and at $x = 470\,\text{mm}$ when moving left to right. This confirms that the direction of travel does indeed shift the position of features in the direction of travel.

Furthermore, a reduction in current on the right side when moving right to left, can be seen. This can be explained by the fact that the driven pattern starts there. The machine drives to the home position in between each pattern, to recalibrate its position. Therefore, the source is moved away from the chamber in between measurements. The reduction in current can be explained by the fact that the source has just been placed in front of the chamber again, further showing that there is delay in the current readout.

Along the movement direction this effect therefore needs to be taken into account in uncertainty considerations, which is described in appendix E. This additional uncertainty is dependent on the step size and the delay between reaching a position and measuring the current.

6 Experimental Results & Discussion

6.1 Initial Measurement Results
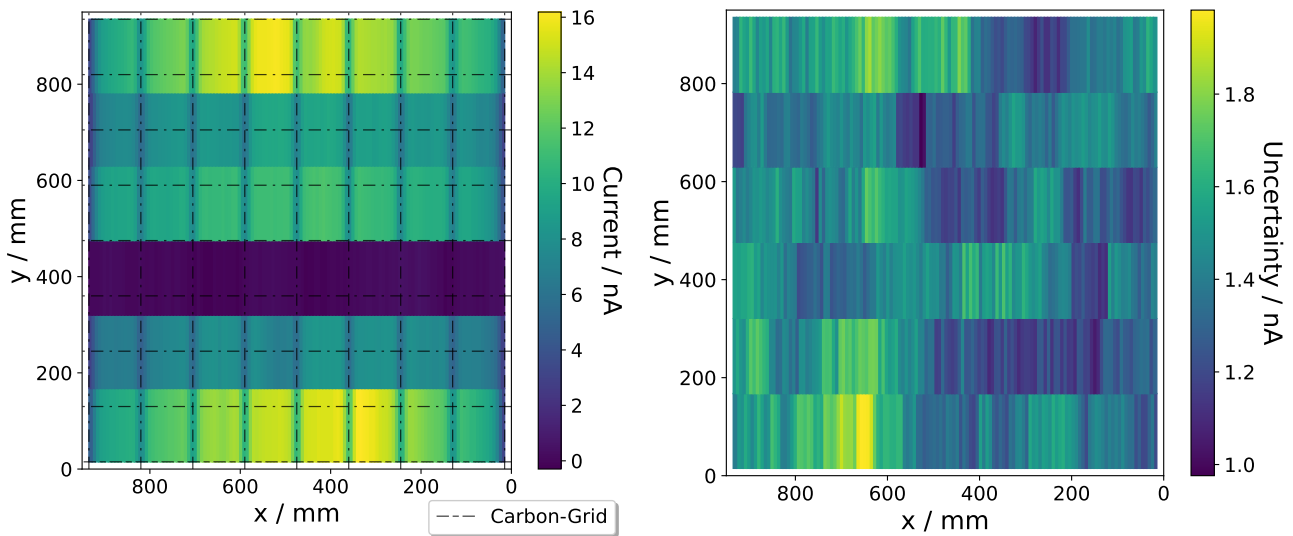
Figure 6.1: Scan 1: Gain measurement at the pad centers of type 8 - chamber 4. Left is the average currents at each location over 56 run cycles, and right the statistical uncertainty, calculated as the standard deviation over 56 run cycles.

Two initial measurements of the gain are taken, using different modes of operation of the control script. Both of these scans serve as a proof of concept showing that results can be achieved with the described setup.

Scan 1 (figure 6.1) measures the gain across the entire active area of the chamber at the pad centers, since the gain scans in later production will particularly be interested in the gain at these positions. Scan 2 (figure 6.2) measures a smaller area with a symmetrical step size of 5 mm both in X and Y direction.

Both scans show an anode current of up to ~16 nA with the turned off section visible in scan 1 clearly showing no gain.

Effects caused by the carbon grid can be observed in both scans and are further compared to the previous approximation in section 6.2. Since in Scan 1 sections 2 and 5 (see section 2.4) lay directly underneath the carbon grid, the entire sections show reduced currents. Furthermore,

a reduction in current in the immediate proximity of the chamber edges can be observed in both scans.

As discussed in section 5.3.2, there is a delay in the current measurement. This causes a repeating pattern along the y-axis in Scan 2, when transitioning between regions effected and not effected by the carbon grid. The delay causes a perceived shift of the lattice along the x-axis in the scan direction. Since the scan runs every second row in the opposite direction (as shown in figure 3.4b) a repeating pattern can be seen that shifts the lattice left/right every second row.

Scan 1 shows some increase towards the center of the chamber along the x-axis, which would be expected with a deformation of the entrance window. This is further discussed in section 6.2.2 but could not be reproduced along the y-axis. Section 4 compared to section 1 and 6 shows a reduced current. This would not be expected from a chamber bulging outwards and is further investigated in section 6.3. Part of the same effect is that in scan 2 an overall reduction towards the top of the scanned area can be observed.
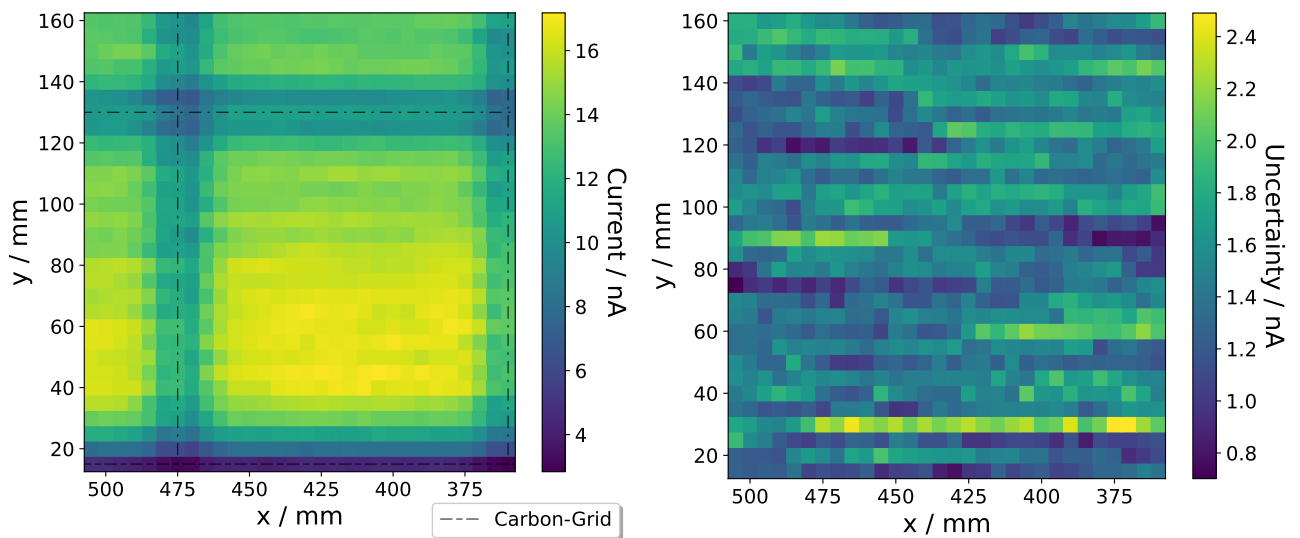
Figure 6.2: Scan 2: Gain measurement across a smaller area at the bottom edge of the chamber. Left are the average currents at each location over 21 run cycles, and right the statistical uncertainty, calculated as the standard deviation over 21 run cycles.

6.2 Comparison to Predicted Effects

6.2.1 Effects caused by the Carbon Grid

Figure 6.3 shows the results generated with the algorithm described in section 4.1 at different distances between the source and chamber. Both the effect at the edge of the chamber and

(a) Results of the approximation close to the chamber edge

(b) Results of the approximation above a lattice grid located at $x = 475\,\text{mm}$

(c) Projection onto the y-axis

(d) Projection onto the x-axis
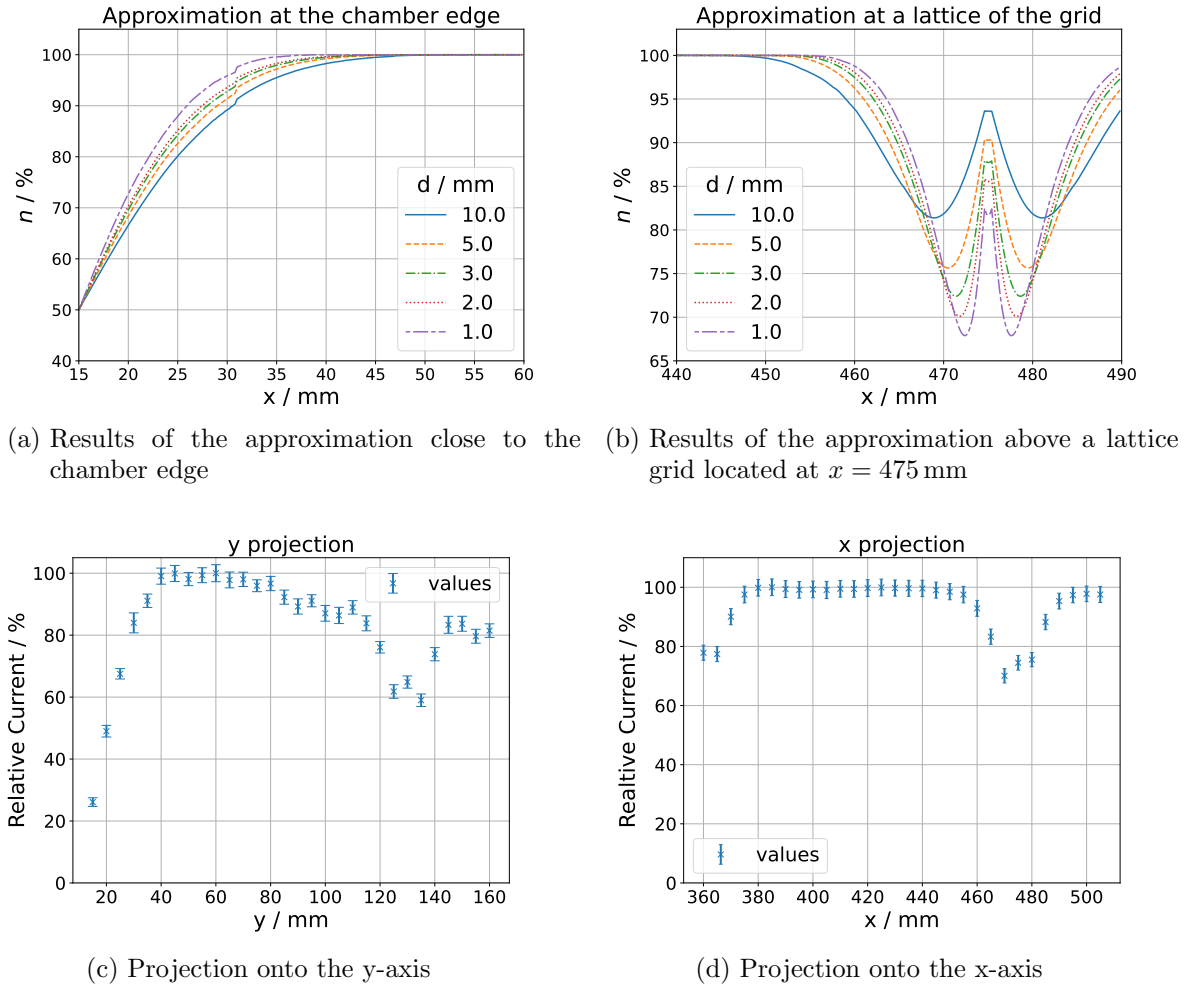
Figure 6.3: (a) and (b) show the results of the numerically calculated approximation described in section 4.1, at different distances d and normalized to the maximum value. Showing the theoretical effect of the chamber edge and the lattice grid when moving across them perpendicularly. As a comparison (c) and (d) show the projection of scan 2 (shown in figure 6.2), which covers one grid section, onto the x and y-axis. This is created by taking the sum over all values long one line and normalizing to the maximum sum over all lines.

over a lattice grid are shown in comparison to real measurements from Scan 2 projected onto the x and y-axis.

Figure 6.3a shows the predicted effects close to the chamber edge. A reduction in the rate of primary ionization can be seen towards the edge of the chamber. Directly over the border of the active area of the chamber (which is at $x = 15\,\mathrm{mm}$ due to the frame of the chamber beeing $15\,\mathrm{mm}$ wide) the reduction is $50\,\%$ independent of the distance. This results from geometric considerations: When beeing directly above the chamber edge, one half of the illuminated area will go past the active volume. With increasing distances, the overall dropoff becomes wider. At all distances, a step at $31\,\mathrm{mm}$ is visible. It is not clear what causes this. With increasing distances, the overall dropoff gets widened, with the drop-off starting between $40\,\mathrm{mm}$ and $50\,\mathrm{mm}$ for all distances.

Figure 6.3b shows the shadowing due to a lattice of the carbon grid. It can be seen that when approaching a lattice perpendicularly, the intensity first reduced but increases again when beeing directly above the grid. This can be explained by the fact that the visible area of the lattice becomes smaller when beeing directly above it, if looked at it from the perspective of the source. Overall, the effect due to the lattice grid becomes greater and narrower with smaller distances to the grid.

In the measurements, due to the fact, that the overall current changes along the y-axis, the effect of the carbon grid can be seen more clearly along the x-axis in figure 6.3d. A reduction between $70\,\%$ and $80\,\%$ can be seen, with the minimum value beeing $(70\pm2)\,\%$ when compared to the maximum value. This aligns with the predicted results of the approximation. The width of the dropoff is approximately $60\,\mathrm{mm}$ which is slightly wider than predicted, which can be explained when considering that there might be further effects caused by the scan pattern and delay in current readout, discussed in section 5.3.2, that cause the width to increased in these results. While in figure 6.3d along the x-axis no significant increase in current directly above the lattice grid, a slight increase can be seen along the y-axis in figure 6.3c. The increase in current is nonetheless smaller than predicted in figure 6.3b. This is likely due to the fact that the ^{55}Fe source is approximated as a point source.

Figure 6.4a shows the results of the algorithm at a grid intersection of the chamber, demonstrating that this approximation can also describe the effects caused by two lattices intersecting in two dimensions. It can be seen that the overall structure with an increase directly above the lattices is repeated. In the corners of the intersections, the effect of the two lattice grids is compounded and leads to a reduction up to $49.6\,\%$ compared to the unaffected areas. The extract of scan 2 displayed in figure 6.4b shows a similar overlap at the intersection of the lattice grid.
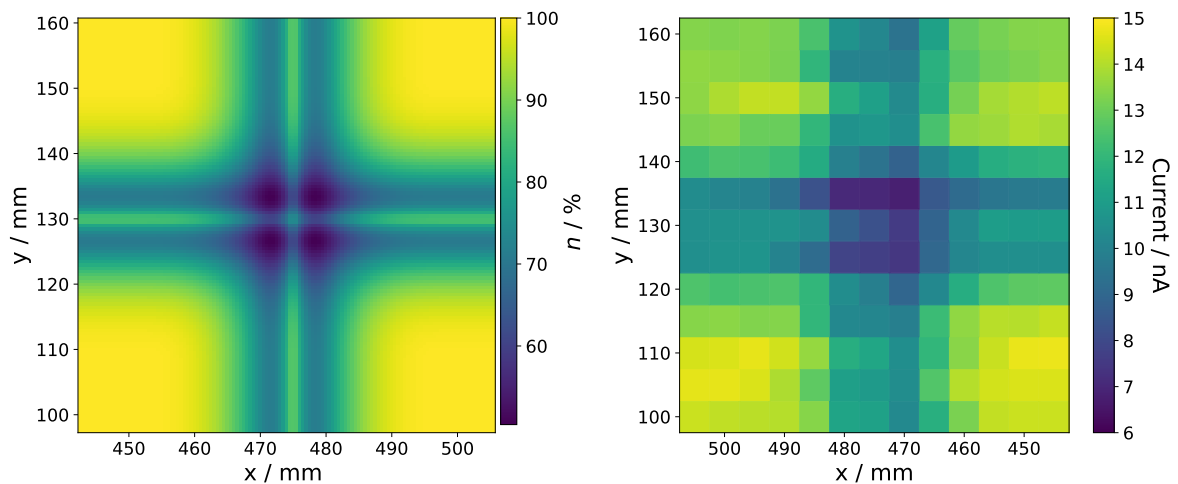
(a) Results of the approximation using the described algorithm at $d = 2.5\,\mathrm{mm}$ showing the effects of an intersection of the lattice grid in x and y direction.

(b) Excerpt from Scan 2 (figure 6.2) showing the measured currents at a grid Intersection.

Figure 6.4

Overall, it can be said that the measured reductions in current are in line with the theoretical approximations. In order to correct for these effects in the gain scans, a better simulation with correct characterization of the ^{55}Fe, would be advisable. Otherwise, only points that are outside the region of influence of these effects should be taken into consideration when determining the uniformity of the gain. Alternatively, points in the effected areas could be compared against other points with the same distance to the grid.

6.2.2 Effects caused by Entrance Window Curvature

Projecting the results from scan 1 (figure 6.1) onto the x-axis and setting the maximum value as $100\,\%$ results in figure 6.5. It can be seen, that, towards the center of the chamber, the current is $100\,\%/70\,\% = 43\,\%$ higher than outer regions of the chamber. Further reductions close to the chamber edges are attributed to some of the illuminated are not hitting the active area, as discussed in section 4.1. As shown in section 4.2 the relationship between change in rate of primary ionizations and deflection of the entrance window is $\Delta n = 0.065 \cdot \Delta d$. Therefor an increase of $43\,\%$ would be a deformation of $6.7\,\mathrm{mm}$. A deflection of this magnitude is significantly greater than indicated design specifications with $1\,\mathrm{mm}$ [8, p.66] or the deformation measured in [21]. When considering the change in gain due to the change in electric field, discussed in [8, p.71, 5.4.3 Electrostatic calculations] the effect of the deflection should be even less visible. This either indicates that the previous approximation in section 4.2 underestimates the magnitude of the effect, or that some further effect is contributing to the visible increase of current towards the center of the chamber. As later discussed in section 6.3
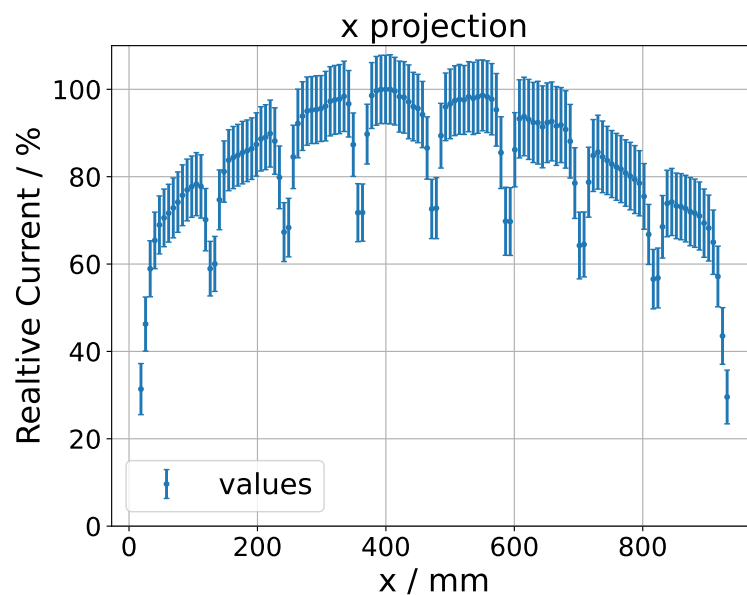
Figure 6.5: Projection onto the x-axis of measurements from Scan 1 (shown in figure 6.1). Shown is the entire width of the chamber. Created by taking the sum over all values over measurements with the same x-position and then setting the largest value to 100 %.

there are two maxima at the bottom and top of the chamber that have not been explained and might contribute to the profile observed here. It is therefore unclear how much of the observed effect actually stems from deformation of the entrance window.

6.3 Discussion of unexpected Effects

Section 4 (see section 2.4) in scan 1 (figure 6.1) shows lower currents than sections 1 and 6. The cause of this is not understood. Two further measurements show this effect in more detail.

Scan 3 in figure 6.6 follows a line in y-direction at $x = 415\,\mathrm{mm}$, which is an area in the middle of the chamber unaffected by the lattice grid. The starting position is chosen directly above the disabled section at, $y = 475\,\mathrm{mm}$ going up until the chamber edge in steps of $1\,\mathrm{mm}$. The resulting currents can be seen in figure 6.6.

Scan 4, shown in figure 6.7, covers the entire active area of the chamber with a step size of $20.5\,\mathrm{mm}$ in x- and y-direction.

Both scans show a dropoff in current at the edge of the chamber and in the immediate vicinity or inside of section 3 which was disabled. This can be explained by part of the illuminated area hitting areas with no gas amplification. Scan 4 only shows this edge effect at the bottom and right edge due to an error in the scan parameters, making the scan skip the last row and
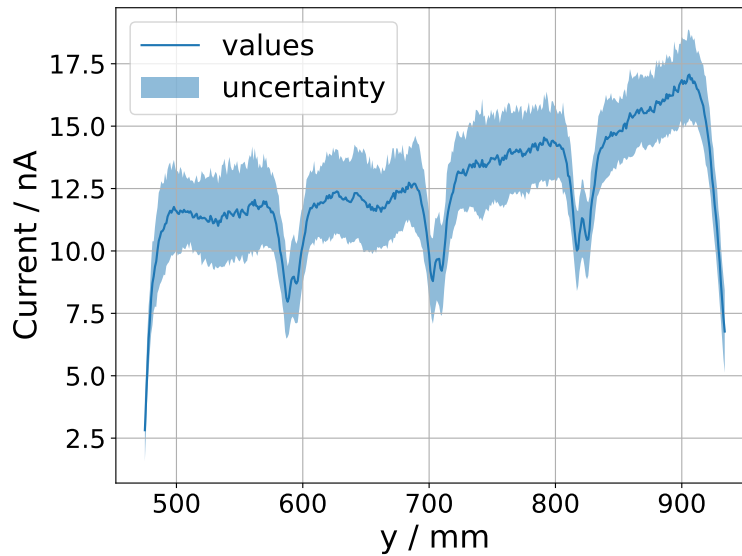
Figure 6.6: Scan 3: Gain measurements across a line along the Y-direction at $x = 415\,\mathrm{mm}$ in 1 mm steps starting just above the disabled section at $y = 415\,\mathrm{mm}$ and going up until the chamber edge. Averaged over 59 scan cycles.

column of the intended scan area. Therefor not taking data points close to the top and left edges.

Also, visible in both scans are the expected dropoffs coinciding with the carbon grid. As predicted in chapter 4 an increase in current when measuring directly above the lattice grid can be seen in Scan 3. Due to the small step size of 1 mm this is visible more clearly than in other scans.

Beyond that, in scan 3 a continuous increase towards the chamber edge, can be observed. This rules out any differences in the section themselves, such as voltage differences in each section, which were unlikely since the sections are wired in parallel. Additionally, The effect is not any effect stemming from a smaller pattern that wasn't captured in earlier scans but is in fact a large scale trend in the chamber.

Scan 4 shows that the increase is symmetrical and appears both towards the top and bottom of the chamber and the effect is concentrated at the center of the top and bottom edges. This creates two maxima at the middle of the top and bottom sides of the chamber, that show 70 % more current when compared to surrounding regions.

The change along the x-axis was previously believed to be the curvature of the chamber window. But as section 4.2 shows, this effect is expected to be smaller than observed. Although the outward curvature along X might have an effect, when considering these results, it is more likely that the change in current along X in the effected regions is part of the same effect observed along the Y-direction.
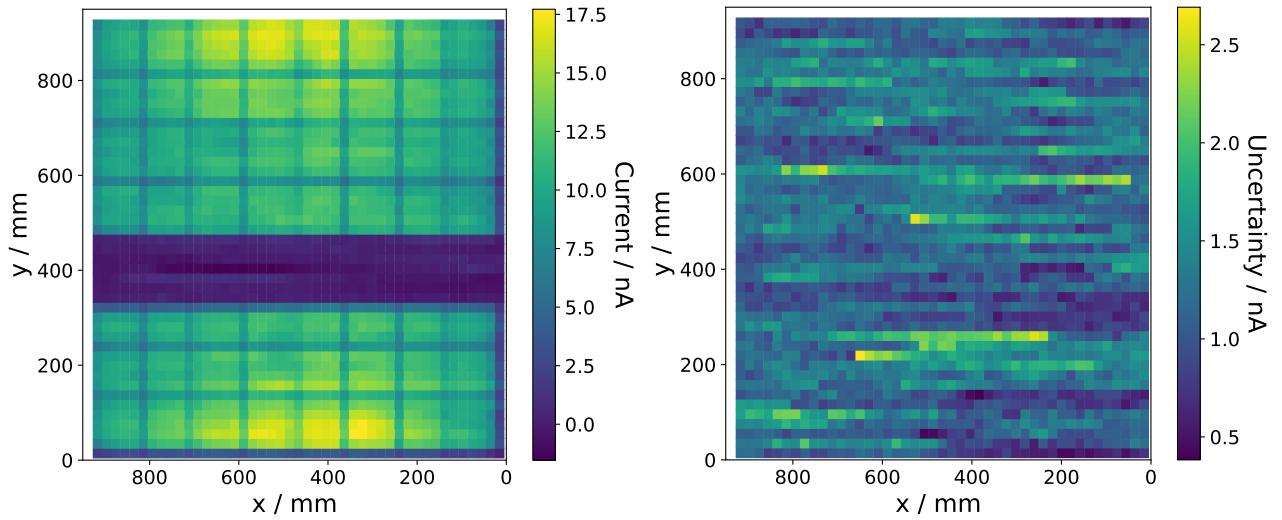
Figure 6.7: Scan 3: Gain measurements across entire active area of the chamber with equal step sizes of 20.5 mm in both X and Y direction. The top and right most lines are skipped due to an error in the scan parameters.

The observed symmetry rules out an effect caused by a misalignment of the chamber position, since the surface describing the scan pattern, as described in section 3.5.1, would not allow for this kind of symmetry to occur. Furthermore, the source would have to move $\ln(1.7)/\mu_{ag} = 18.8$ cm in the z-direction to cause a 70 % change in current. This is larger than the travel range of the CNC-Machine in the z-direction and is therefor not possible.

A curvature of the entrance window could be an explanation. As discussed in section 4.2 an outward curvature of the chamber would increase the rate of primary ionizations towards the center of the chamber. This is indeed the opposite of what is observed here. Since an inward curvature of the entrance window is unlikely, it is assumed that the effect is not a change in the rate of primary ionization, but an actual change in gain.

As discussed in [8, p. 72: 5.4.3 Electrostatic calculations] an outward curvature can cause a change in gain by changing the electric field in the chamber. The simulation predicts a reduction in gain of 6 % per 1 mm curvature, which is significantly less than observed here. But as discussed in section 4.2 the effect was simulated at 1850 V anode and −500 V drift voltages.

Therefor a further measurement is performed to show the observed effect at different voltages. For this courser scans with positions at each center of the entrance windows formed by the carbon grid are performed at anode voltages of 1870 V, 1930 V, 1990 V. The results are visible in figure 6.8. At lower voltages, the baseline is reduced and as predicted in section 2.2 the overall measured gain and therefore also the current is reduced. With the lower current, the signal-to-noise ratio worsens, leading to a higher relative uncertainty at 1860 V. Although

(a) Current at 1870 V   (b) Current at 1930 V   (c) Current at 1990 V

(d) Uncertainty at 1870 V   (e) Uncertainty at 1930 V   (f) Uncertainty at 1990 V
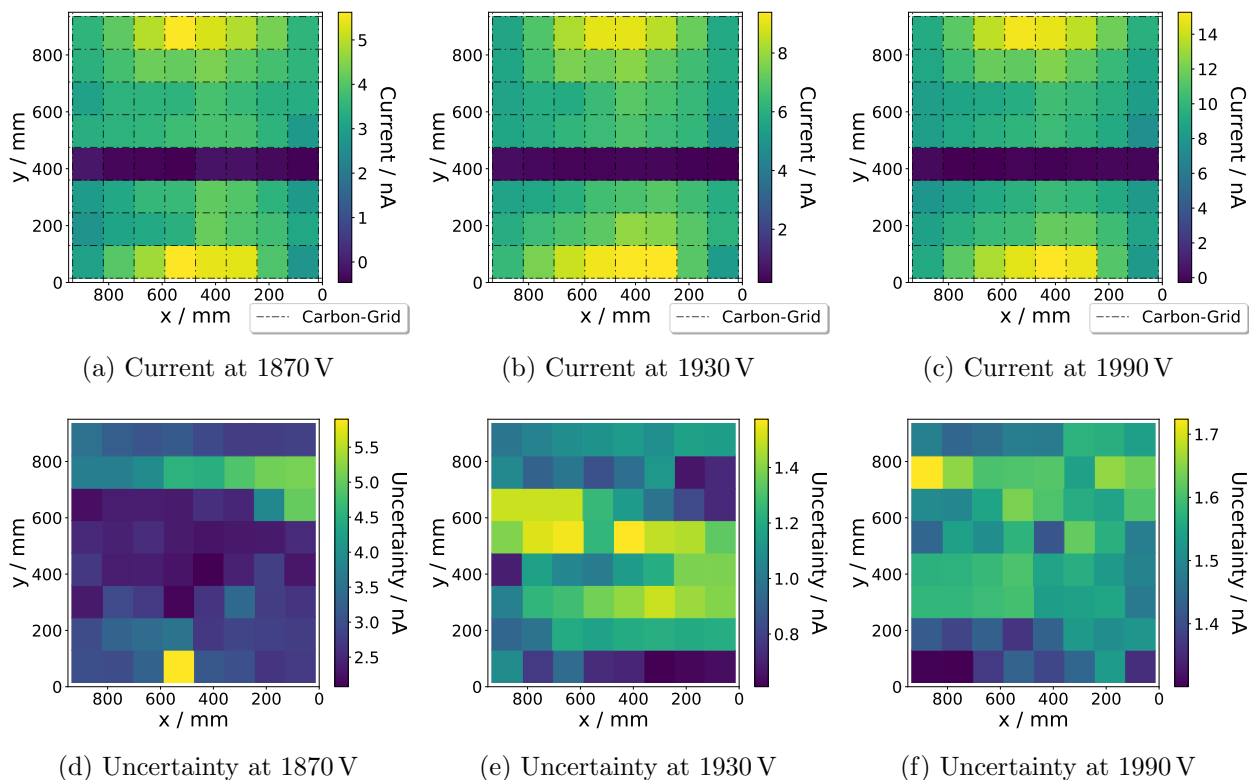
Figure 6.8: Multiple Scans of the chamber at different anode voltages of 1870 V, 1930 V and 1990 V and a drift voltage of 400 V. The scan positions are chosen as the centers of the separate windows created by the lattice grid.

this is the case, the same overall pattern with two maxima at the top and bottom edges can be seen.

The effect is most likely neither a scan artifact nor is it voltage dependent. Considerations were made into whether the fact, that the anode wires of the disabled section are not grounded could lead to a collection of charge disturbing the electric field of the chamber. To test this theory further measurements, in which the wires are grounded, are needed.

6.4 Uniformity Calculations

As a measure of the uniformity of the measured gain map, the coefficient of variation defined as σ/μ over all measured positions is calculated [25]. With $\mu = 1/N \sum_{i=1}^{N} I_i$ beeing the average current over all currents at N positions and $\sigma = \sqrt{\sum_{i=1}^{N} (I_i - \mu)^2 / N}$ beeing the standard deviation over all calculated positions.

The issue with the approach is, that any of the effects discussed in section 4.2 might contribute to the overall deviation in the measured current.

Table 6.1: Uniformity calculations for all performed scans showing the positions taken into account, the overall size of the bounds of the scanned area and the resulting average of the current over all positions, the standard deviation and coefficient of variation.

	Positions	Area / mm²	μ/nA	σ/nA	σ/μ / %
Scan 1	240	870×768	11.98	2.21 ± 0.09	18.5 ± 0.5
Scan 2	256	120×120	15.54	1.14 ± 0.09	7.3 ± 0.6
Scan 3	260	0×406	13.3	1.7 ± 0.1	13.1 ± 0.8
Scan 4	546	840×840	12.11	1.98 ± 0.04	16.4 ± 0.4
1870V	48	805×805	3.9	0.7 ± 0.5	19 ± 12
1930V	48	805×805	6.9	1.1 ± 0.1	16 ± 2
1990V	48	805×805	10.6	2.0 ± 0.2	19 ± 2

For the deformation of the entrance window the amount of the effect contributes can be approximated by, assuming that the window describes a parabola across the entire with of the entrance window with $y = 1\,\text{mm}$ as the maximum and $y = 0\,\text{mm}$ at the edge of the window and the change in gain is described by $6.4\,\% \cdot h$ in accordance with equation (4.5). Calculating the coefficient of variation shows that effect entrance window will contribute approximately 1.83 *p.p.* to the coefficient of variation.

For the effects caused by the carbon grid, a better description would be needed, in order to correct for the effects. To avoid this issue, all measurements taken within 25 mm of the carbon grid are not included. Furthermore, all measurements taken in the disables Section of the measured chamber are not included in the calculation, since it was consciously turned off.

Calculating the coefficient of variation for all the performed scans results in table 6.1. Due to the still unexplained effect discussed in section 6.3, it can be seen that for most scans the coefficient of variation lays between 16 % and 19 nA. Without this effect the coefficient would likely be significantly smaller. Since the effect observed spans larger distances, in scans that cover smaller areas, in particular scans 2 and 3, the coefficient of variation is lower. Scans that cover most of the chamber's active area the uncertainty of the results is governed by the number of scanned positions and the voltage which directly influences the amount of current measured. These results all lay withing the region of 16 % and 19 %, with some scans showing differences beyond their uncertainties. This is likely due to the fact that they do cover the chamber in different patterns.

7 Conclusion and Outlook

As outlined in the previous chapters, gain scans of MWPC chambers for the CBM TRD have been implemented and commissioned using an existing type 8 chamber. A program for performing these scans has been developed is available on GIT. Documentation and instructions for operating this program is still in work and will be finished shortly. There are a number of possible improvements to be made to the current setup, which are discussed in the following.

Overall results show currents up to $17\,\text{nA}$ across the active area of the chamber which were measured with a spatial resolution of up to $6\,\text{mm}$. Effects caused by absorption of the carbon grid in front of the chamber were observed and theoretical estimations of the effect were consistent with the measurements. Further approximations of the effects on the measurements due to the curvature of the entrance window were performed, but could not be definitively shown to match with actual measurement results. This is due to an increase in the measured currents at the top and bottom edges of the test chamber. This effect is still unexplained. Further measurements to test possible explanations are needed.

The first type 5 chamber has been completed as of writing this thesis and is ready for gain scans. Which will hopefully begin in the coming weeks. With production of the chambers ramping up, regular gain scans will then be performed as chambers are finished, with each scan taking approximately 1 to 2 days depending on the desired quality of the scan.

Based on the work described as part of this thesis and the results presented in chapter 6 a number of possible improvements to the gain measurement setup are proposed. Especially improvements in the way the current is measured and in the intensity of the source are recommended.

As shown in section 5.3, the current readout with the ISEG power supply shows significant limitations, especially when encountering low leakage currents. A separate current meter that is more suitable for this application could therefor be neccecarry to perform future scans.

With an intensity of $5\,\text{MBq}$, the selected ^{55}Fe source is significantly weaker than its original intensity of $37\,\text{Mbq}$. A source with higher intensity with at least $20\,\text{Mbq}$ would increase the amount of current received and therefor improve the signal-to-noise ratio. A stronger

source could additionally allow for a trade-off between the increased intensity and a smaller collimator that intern would increase the spatial resolution of the scans.

It was shown that the script automating the measurements is operational with the currently chosen scan parameters. To improve both the efficiency of the script and the quality of the results, a detailed analysis of the scan parameters would be beneficial. This includes the baseline interval, step delay and number of scan cycles against the time needed to perform the scan.

A better description of the effects caused by the carbon grid would be helpful in correcting for the effects and would therefor allow uniformity calculations across a wider area of the chamber. To realize this, a better description of the profile of the used source would also be helpful. Measuring this directly with a pixel detector would be one option but still might not correctly describe the size of the source itself. Alternatively, the uniformity calculations could be done with a different approach, in which comparison between the same positions relative to the lattice grid are made.

Appendix

A   Chamber Geometry
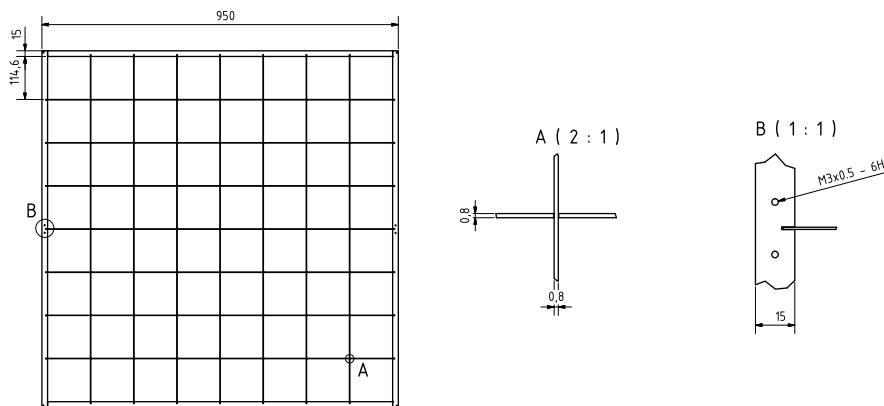
A.1   Lattice Grid and Frame

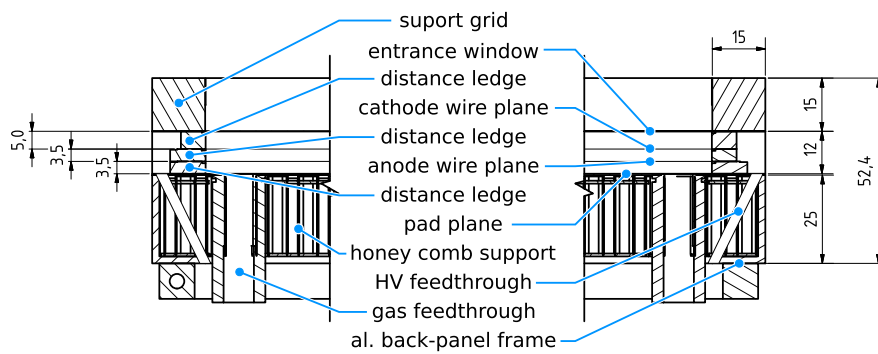Figure A.1: Layout of the carbon grid [8, p. 67, fig. 5.12]

Figure A.2: Cross-section showing the measurements of the frame and depth of the carbon grid. [8, p. 65, fig. 5.10]

A.2 Pad plane layout / Chamber Types

Table A.1: Number of Pads, pad dimensions and active area of different chamber types ([8, p. 72, table 5.4]) for types 1-7 and [24] for type 8)

Type	Columns	Rows	Pad Height (cm)	Pad Width (cm)	Active Area (cm^2)
1	80	32	1.75	0.68	54×54
3	80	8	6.75	0.68	54×54
5	144	24	4.00	0.67	96×96
7	144	8	12.00	0.67	96×96
(8)	128	6	$A = 15.25$ $B = 15.5$	0.72	92×92

The type 8 chamber consists of pads with two different heights arranged in an A-A-B-B-A-A layout.

B Derivation of Plane Correction

With a (4×4) quaternion matrix, translation, rotation and scaling of objects in 3d-space can be achieved [26]. This allows the x-y-plane in the chamber system that describes the front of the chamber to be transformed with:

$$\vec{r}_{pc} = T_{4\times4} \cdot \begin{pmatrix} x_{cs} \\ y_{cs} \\ 0 \\ 1 \end{pmatrix} - \begin{pmatrix} 0 \\ 0 \\ z_{cs} \\ 0 \end{pmatrix} \tag{B.1}$$

The z-coordinate is treated differently, as described in section 3.5.1. Since the last row of the vector is not needed for $\vec{r}_{pc}$ and due to the 0 in $\begin{pmatrix} x_{cs}, & y_{cs}, & 0, & 1 \end{pmatrix}^T$ this can be simplified to:

$$\vec{r}_{pc} = T_{3\times3} \cdot \begin{pmatrix} x_{cs} \\ y_{cs} \\ 1 \end{pmatrix} - \begin{pmatrix} 0 \\ 0 \\ z_{cs} \end{pmatrix} \tag{B.2}$$

C Derivation of Y-Correction

Assuming that the four corners of the chamber are connected by straight edges, results in the following description of the z-correction along the edges:

$$z(0, y) = (z_2 - z_1) \cdot \frac{y}{t} + z_1 \qquad z(l, y) = (z_3 - z_4) \cdot \frac{y}{t} + z_4 \tag{C.1}$$

$$z(x, 0) = (z_4 - z_1) \cdot \frac{x}{l} + z_1 \qquad z(x, t) = (z_3 - z_2) \cdot \frac{x}{l} + z_2 \tag{C.2}$$

$$\tag{C.3}$$

With $z(0,0) = z_1$, $z(0,t) = z_2$, $z(l,t) = z_3$, $z(l,0) = z_4$ being the actual z-position of the corners in the machine system, l being the x-position of the left edge in the machine system, r being the y-position of the top edge in the machine system and with the right and bottom edges being at 0 each.

Linear interpolation between two opposite sides (here the interpolation between the horizontal edges):

$$z(x, y) = (z(x, t) - z(x, 0)) \cdot \frac{y}{t} + z(x, 0) \tag{C.4}$$

$$= ((z_3 - z_2) \cdot \frac{x}{l} + z_2 - (z_4 - z_1) \cdot \frac{x}{l} - z_1) \cdot \frac{y}{t} + (z_4 - z_1) \cdot \frac{x}{l} + z_1 \tag{C.5}$$

$$= \underbrace{\frac{z_3 - z_2 - z_4 + z_1}{l \cdot t}}_{p_1} \cdot xy + \underbrace{\frac{z_2 - z_1}{t}}_{p_2} \cdot y + \underbrace{\frac{z_4 - z_1}{l}}_{p_3} \cdot x + \underbrace{z_1}_{p_4} \tag{C.6}$$

$$= p_1 \cdot xy + p_2 \cdot y + p_3 \cdot x + p_3 \tag{C.7}$$

Finally, with $x_{zc} = x_{pc}$, $y_{pc} = y_{zc}$ and including the z-coordinate this can be written as:

$$\vec{r}_{zc} = \begin{pmatrix} 1 & 0 & 0 & 0 \\ 0 & 1 & 0 & 0 \\ p_1 & p_2 & p_3 & p_4 - z_{cs} \end{pmatrix} \cdot \begin{pmatrix} x_{pc} \\ y_{pc} \\ x_{pc} \cdot y_{pc} \\ 1\,\mu m \end{pmatrix} \tag{C.8}$$

D Fit Parameters describing the Chamber Position

All shown scans were performed with the chamber position beeing described in accordance with section 3.5.1, using the parameters:

$$T_{pc} = \begin{pmatrix} 1.0000 & 6.3998 \times 10^{-3} & 1.1500 \times 10^5 \\ -9.3654 \times 10^{-3} & 1.0003 & 2.0807 \times 10^5 \\ 4.9409 \times 10^{-3} & 1.0973 \times 10^{-2} & 9.8081 \times 10^4 \end{pmatrix} \tag{D.1}$$

and

$$p_1 = (2.4 \pm 0.4) \times 10^{-3} \tag{D.2}$$

$$p_2 = (8.8 \pm 0.4) \times 10^{-4} \tag{D.3}$$

$$p_3 = (2.3 \pm 0.6) \times 10^{-9} \tag{D.4}$$

$$p_4 = (9.90 \pm 0.02) \times 10^2 \tag{D.5}$$

resulting in an z-uncertainty of under $\pm 0.2\,\mathrm{mm}$ in the area of the active area of the chamber.

E   Derivation of Source Intensity

The intersection of two circles with identical radii R and the distance d can be written as [23]:

$$A = 2R^2 \cos^{-1}\left(\frac{d}{2R}\right) - \frac{1}{2}d\sqrt{4R^2 - d^2} \tag{E.1}$$

When looking at a cylinder from a large distance at the angle φ, the circular top and bottom of the cylinder are compressed by a factor of $cos(\varphi)$ and the distance d between the centers of the top and bottom appears to be $d_{coll.} \cdot sin(\varphi)$. In order to apply the circle intersection equation the image is stretched by $1\cos\varphi$. Therefor $d = d_{coll} \cdot |\tan\varphi|$ and $R = r_{col.}$.

$$I_0(\varphi) = 2r_{\mathrm{col}}^2 \cdot \cos^{-1}\left(\frac{d_{\mathrm{col}}}{2r_{\mathrm{col}}} \cdot |\tan(\varphi)|\right) - \frac{1}{2} \cdot d_{\mathrm{col}} \cdot |\tan(\varphi)| \cdot \sqrt{4r_{\mathrm{col}}^2 - (d_{\mathrm{col}} \cdot \tan(\varphi))^2} \tag{E.2}$$

F Derivation of Influence of the Chamber Deformation on the Uniformity

Assuming that $h(x) = 1 - x^2$ is the deflection height of the entrance window and $g(x) = 0.064h(x) + 1$ (see section 4.2) being the relative gain inside the chamber. It can be calculated that

$$\mu = \frac{1}{2} \int_{-1}^{1} g(x) dx \tag{F.1}$$

$$= \int_{0}^{1} 1.064 - 0.064 x^2 dx \tag{F.2}$$

$$= 1 + \frac{2}{3} 0.064 = 1.0426 \tag{F.3}$$

And

$$\sigma = \frac{1}{2} \int_{-1}^{1} (g(x) - \mu)^2 dx \tag{F.4}$$

$$= 0.064^2 \int_{0}^{1} (\frac{1}{2} - x^2)^2 \tag{F.5}$$

$$= 0.064^2 (\frac{1}{5} - \frac{1}{9}) = 0.01908 \tag{F.6}$$

Therefor:

$$\sigma/\mu = 1.830\,\% \tag{F.7}$$

G Uncertainty Considerations

All uncertainty considerations were done in accordance with the *Guide to the expression of uncertainty min measurements* (GUM) [27].

The main concepts used are:
Triangular Distributions width the width a:

$$u = \frac{a}{2\sqrt{6}} \tag{G.1}$$

Rectangular Distributions width the width a:

$$u = \frac{a}{2\sqrt{3}} \tag{G.2}$$

Combination of Uncertainties u_1, u_2, ... u_n:

$$u = \sqrt{\sum_{i=0}^{N} u_i^2} \tag{G.3}$$

Error Propagation for a function $f(x_1, x_2, ..., x_N)$:

$$u_f = \sqrt{\sum_{i=1}^{N} \left(\frac{\partial f(x_i)}{\partial x_i} u_{x_i}\right)^2} \tag{G.4}$$

G.1   Spatial Uncertainty

Z-Uncertainty

When determining the Z-Position in the machine System, which is equivalent to the distance between the chamber and the front of the ^{55}Fe source, the uncertainty stemming from the z-calibration, which is $\pm 0.2\,\text{mm}$, the uncertainty given by the manufacturer of the CNC machine, which is $0.01\,\text{mm}$ and the precession when mounting the ^{55}Fe into the mount of the machine, which is assumed to be $1\,\text{mm}/\sqrt{24} = 0.4\,\text{mm}$ with triangle distribution.

Therefor:
$$u_z = \sqrt{(0.2\,\text{mm})^2 + (0.01\,\text{mm})^2 + (0.2\,\text{mm})^2} = 0.3\,\text{mm} \tag{G.5}$$

X-Y Resolution

For the x-y-uncertainty of the illuminated area of the chamber given as $31\,\text{mm}/\sqrt{24} = 6\,\text{mm}$ and the effects caused by the delay in current measurements given as is taken into account. The effect of delay u_t is dependent on the delay t_{wait} after moving and the step size s and is approximated by using the full width half maximum

$$u_t = t_{1/2} \cdot \frac{s}{t_{wait}} \cdot \frac{2}{2.355} \tag{G.6}$$

$$u_y = 6\,\text{mm} \qquad\qquad u_x = \sqrt{(6\,\text{mm})^2 + (u_t(t_{wait,s}))^2} \tag{G.7}$$

This results in $u_x = 7\,\text{mm}$ for Scan 1, $u_x = 6\,\text{mm}$, for Scan 2, $u_x = 12\,\text{mm}$ for Scan 3 and $60\,\text{mm}$ for figure 6.8.

G.2   Current Uncertainty

For all current measurements the shown uncertainty results for repeated measurements at different times over multiple scan cycles. The uncertainty is then calculated as the standard deviation over all the measurements with *Numpy's* standardization function in accordance with:

$$\sigma = \sqrt{\sum_{i=1}^{N} \frac{I_i - \overline{I}}{N}} \tag{G.8}$$

Additionally, the uncertainty of the current readout given by the manufacturer is not shown in the plots but might have to be considered.

G.3   Error Propagation

Half-life of Delay

With $a \cdot e^{-b} + c$ the Half-life is defined as:

$$t_{1/2} = \frac{\ln 1/2}{-b} = \frac{\ln 2}{b} \tag{G.9}$$

The uncertainty for $u_{t_{1/2}}$ is therefor:

$$u_{t_{1/2}} = \left| \frac{\partial t_{1/2}}{\partial b} \cdot u_b \right| = \frac{ln(2)}{b^2} \cdot u_b \tag{G.10}$$

With $b_{\mathrm{for}} = (0.54 \pm 0.03)\,\mathrm{s}^{-1}$ it follows that $t_{1/2} = (1.28 \pm 0.07)\,\mathrm{s}$ and with $b_{\mathrm{back}} = (0.56 \pm 0.03)\,\mathrm{s}^{-1}$ it follows that $t_{1/2} = (1.24 \pm 0.07)\,\mathrm{s}$

Uniformity Calculations

Starting from the currents I_i measured at all viable positions $i = 1, ..., N$ and the uncertainty of the current u_i. The average current μ and the standard deviation over all positions are calculated as:

$$\mu = \frac{1}{N} \sum_{i=1}^{N} I_i \qquad\qquad \sigma = \sqrt{\sum_{i=1}^{N} \frac{I_i - \mu}{N}} \tag{G.11}$$

Using error propagation the uncertainty of σ/μ can then be described as

$$u_{\sigma/\mu} = \frac{1}{2\sigma} \cdot \sqrt{\sum_{i=1}^{N} \left(\frac{2}{N}(I_i - \mu) \cdot u_i \right)^2} \qquad \text{(G.12)}$$
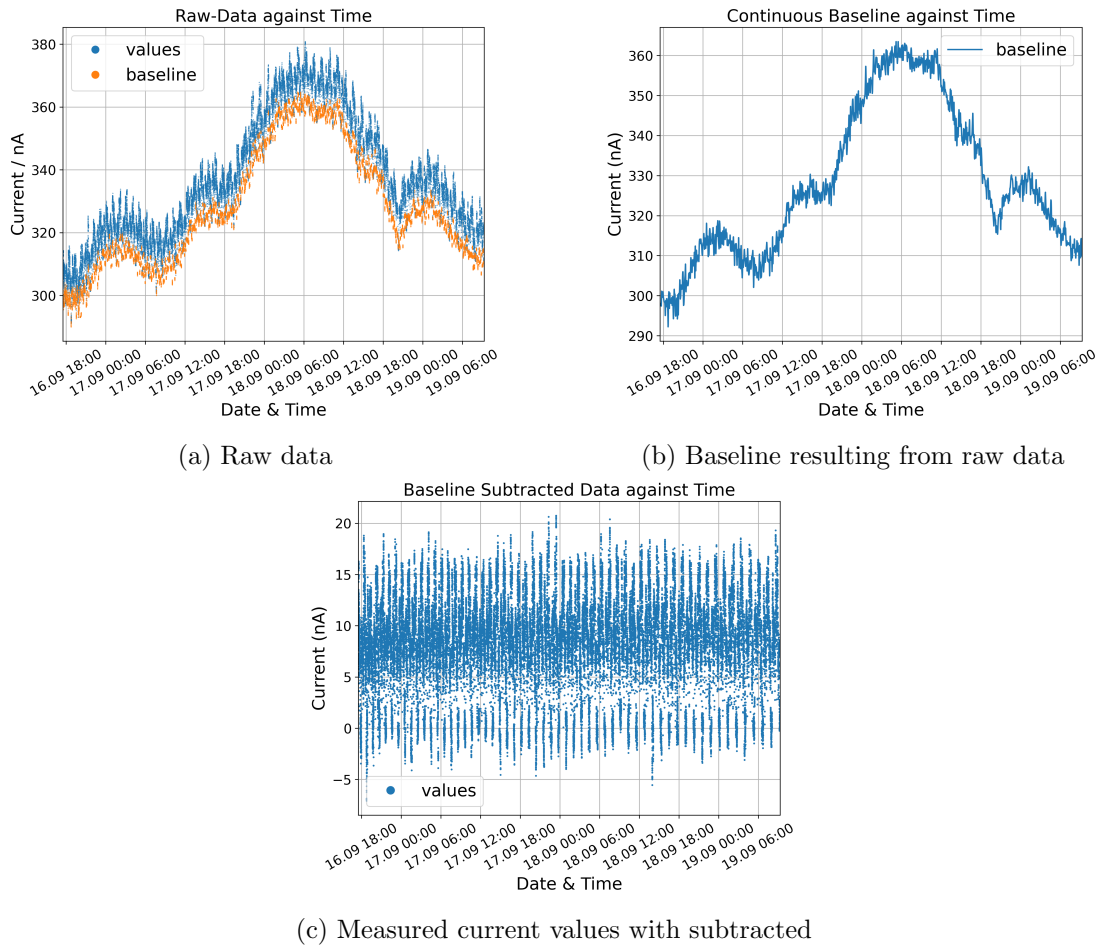
H   Figures and Plots

Scan 1

(a) Raw data

(b) Baseline resulting from raw data

(c) Measured current values with subtracted

Figure H.1: Plots showing the processing steps of scan 1 that result in figure 6.1

(a) Gain map showing the current at all positions considered in the uniformity calculations

(b) Histogram of all currents considered in the uniformity calculations
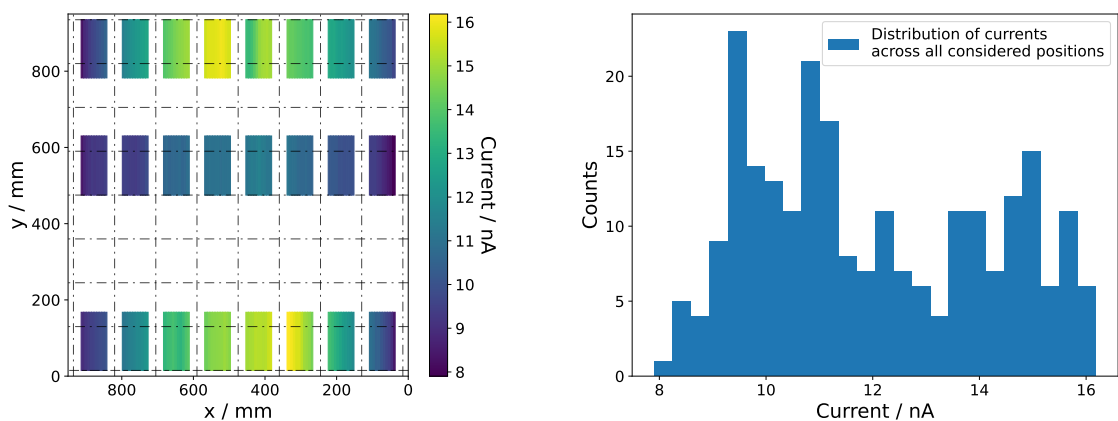
Figure H.2: Plots showing the data used in the uniformity calculations for scan 1

Scan 2

(a) Raw data

(b) Baseline resulting from raw data

(c) Measured current values with subtracted
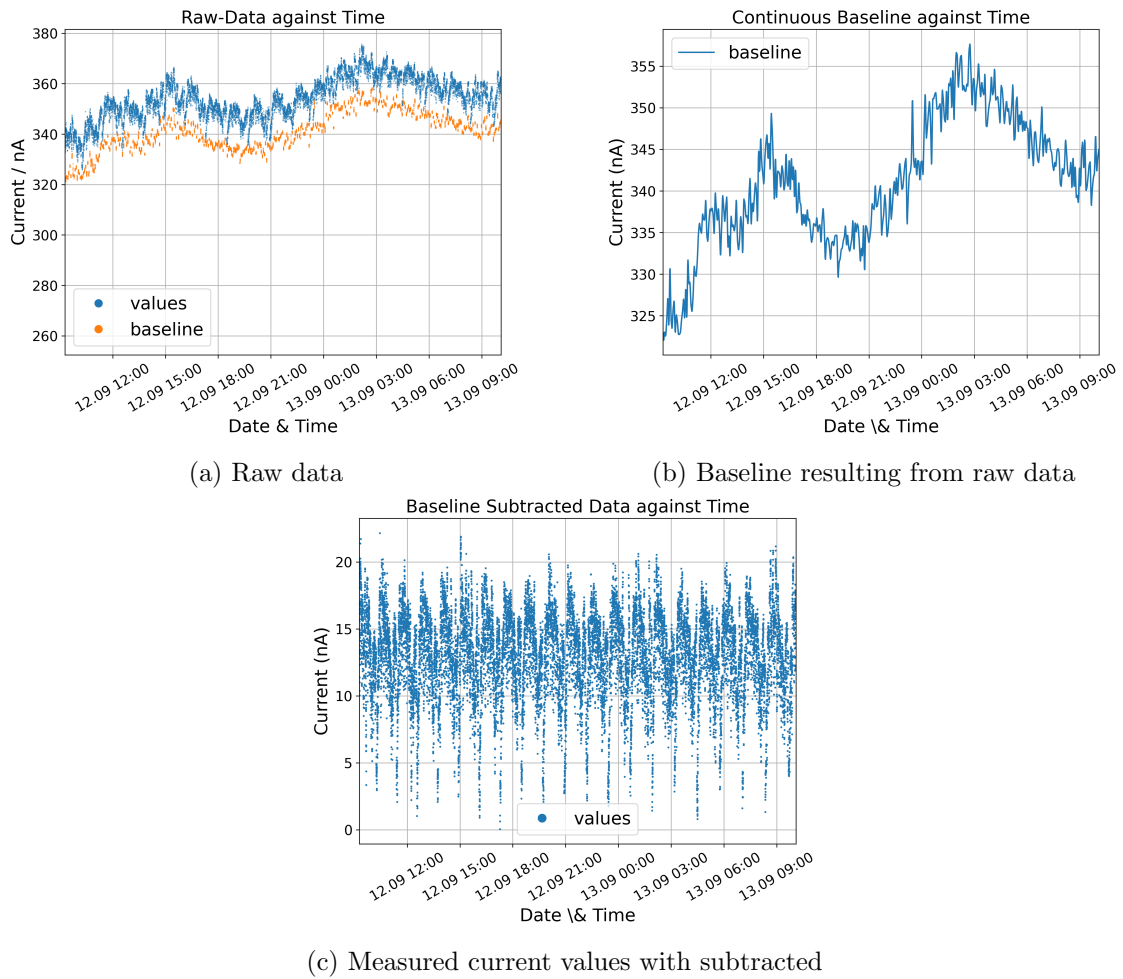
Figure H.3: Plots showing the processing steps of scan 2 that result in figure 6.2

(a) Gain map showing the current at all positions considered in the uniformity calculations

(b) Histogram of all currents considered in the uniformity calculations
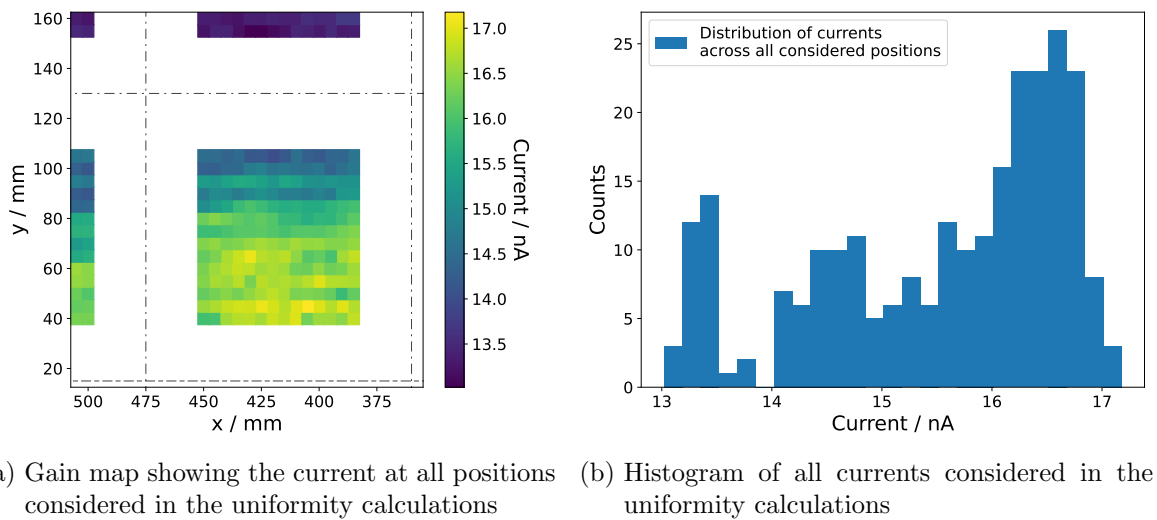
Figure H.4: Plots showing the data used in the uniformity calculations for scan 2

Scan 3

(a) Raw data

(b) Baseline resulting from raw data

(c) Measured current values with subtracted
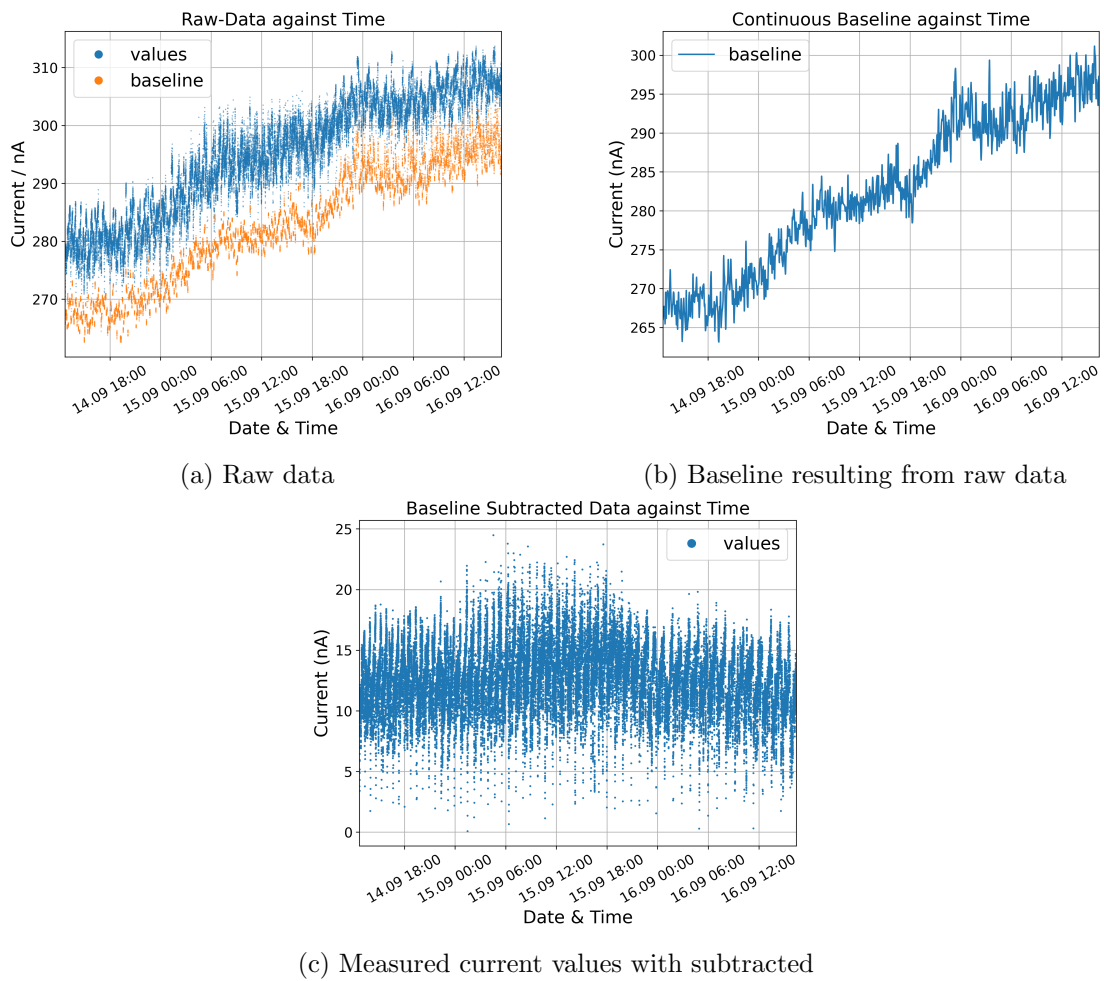
Figure H.5: Plots showing the processing steps of scan 3 that result in figure 6.6

(a) Gain map showing the current at all positions considered in the uniformity calculations

(b) Histogram of all currents considered in the uniformity calculations
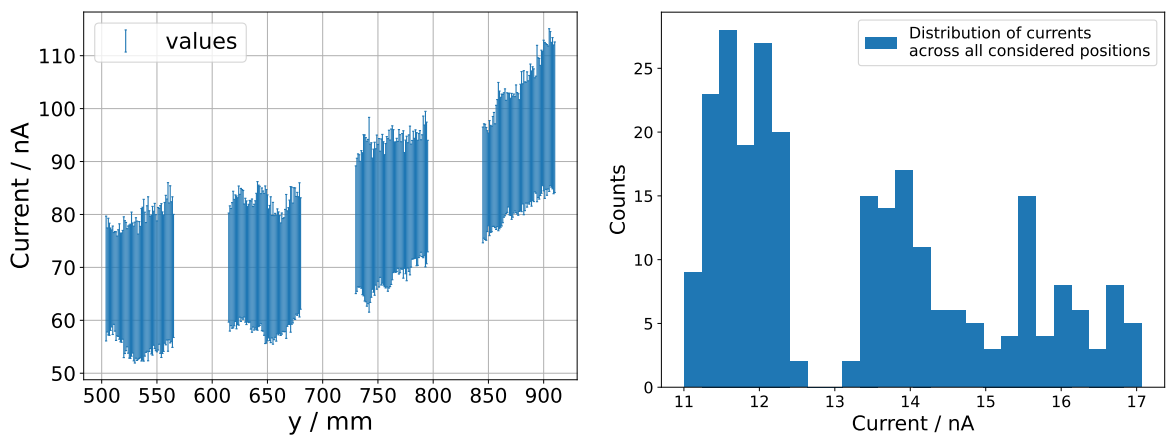
Figure H.6: Plots showing the data used in the uniformity calculations for scan 3

Scan 4

(a) Raw data

(b) Baseline resulting from raw data

(c) Measured current values with subtracted
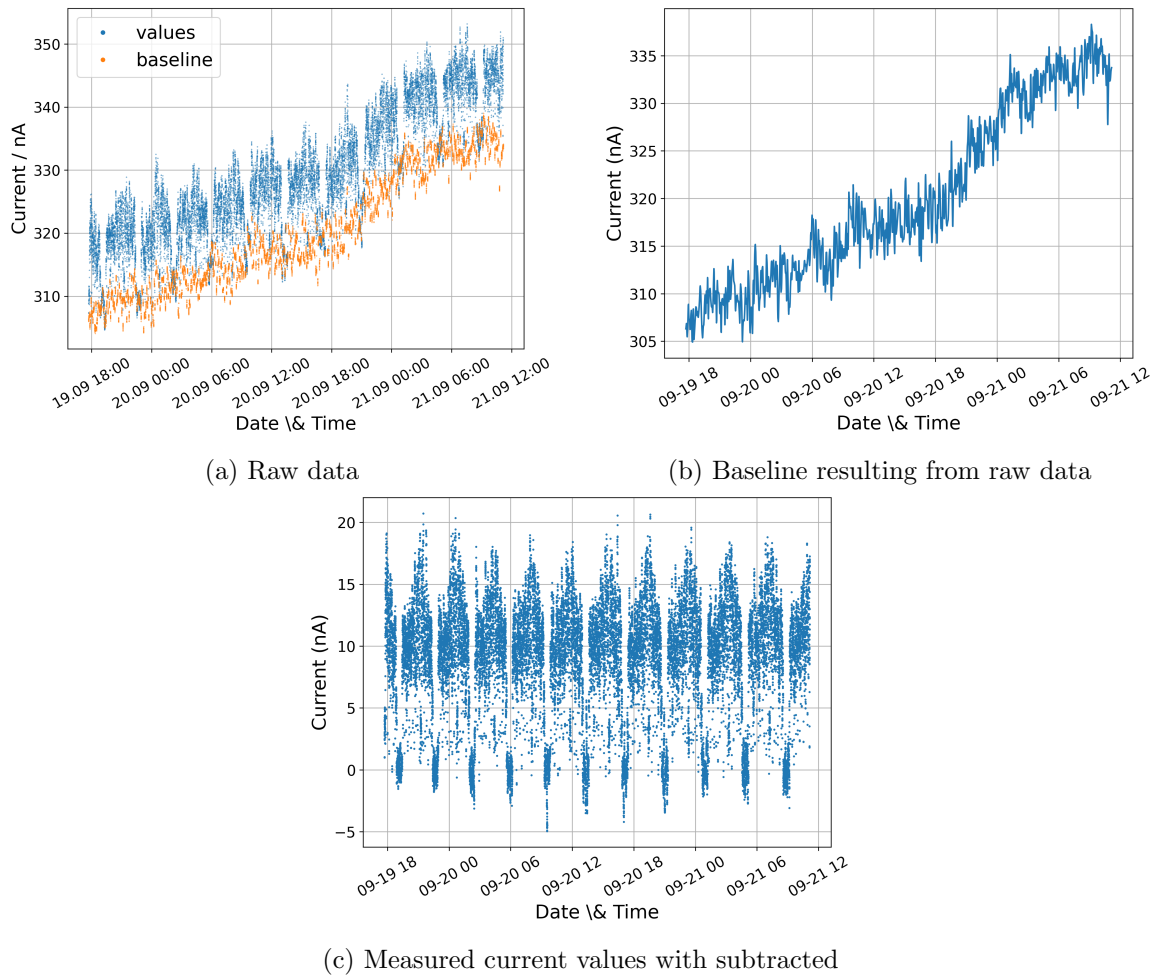
Figure H.7: Plots showing the processing steps of scan 4 that result in figure 6.7

(a) Gain map showing the current at all positions considered in the uniformity calculations

(b) Histogram of all currents considered in the uniformity calculations
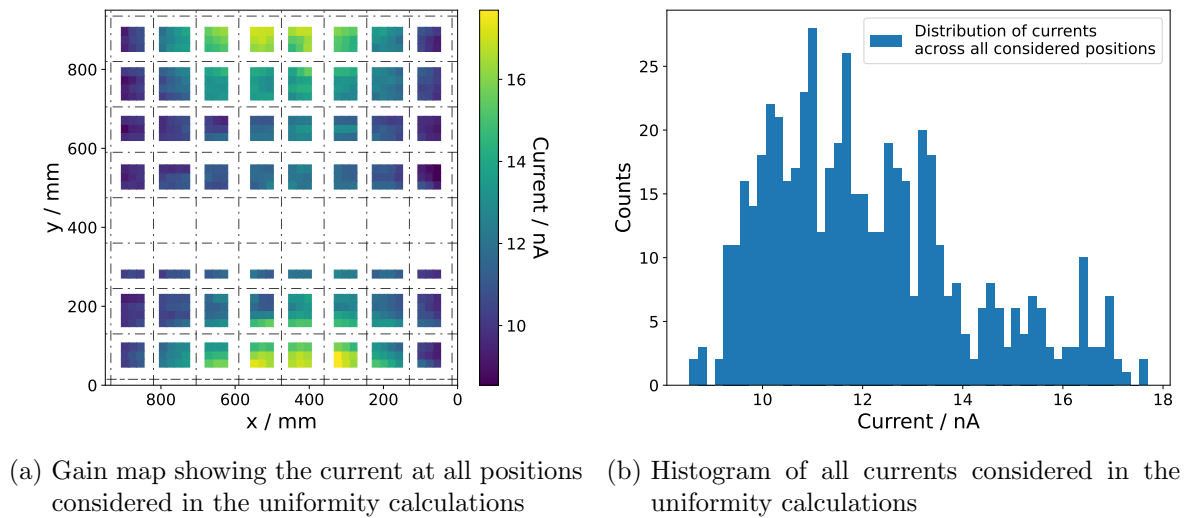
Figure H.8: Plots showing the data used in the uniformity calculations for scan 4

Scan at 1870 V

(a) Raw data

(b) Baseline resulting from raw data

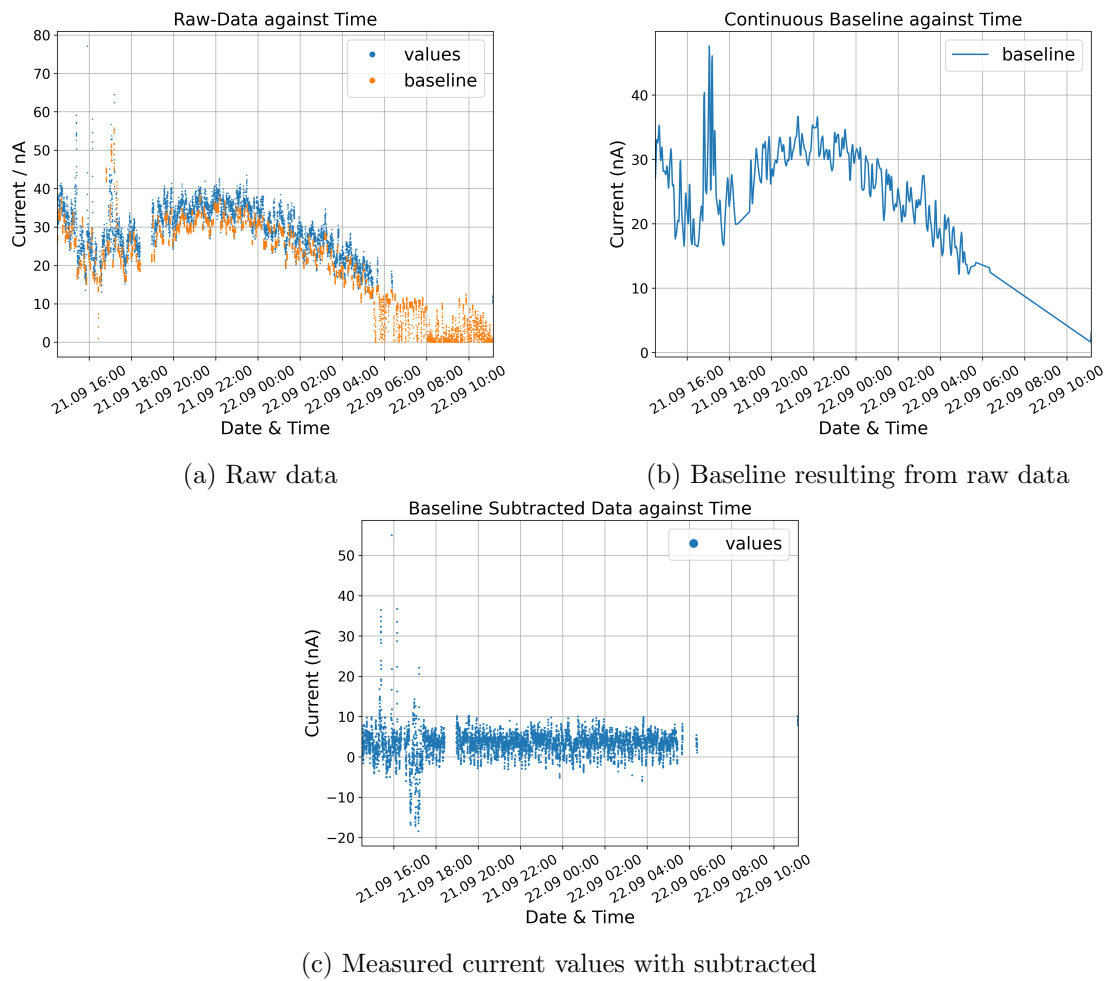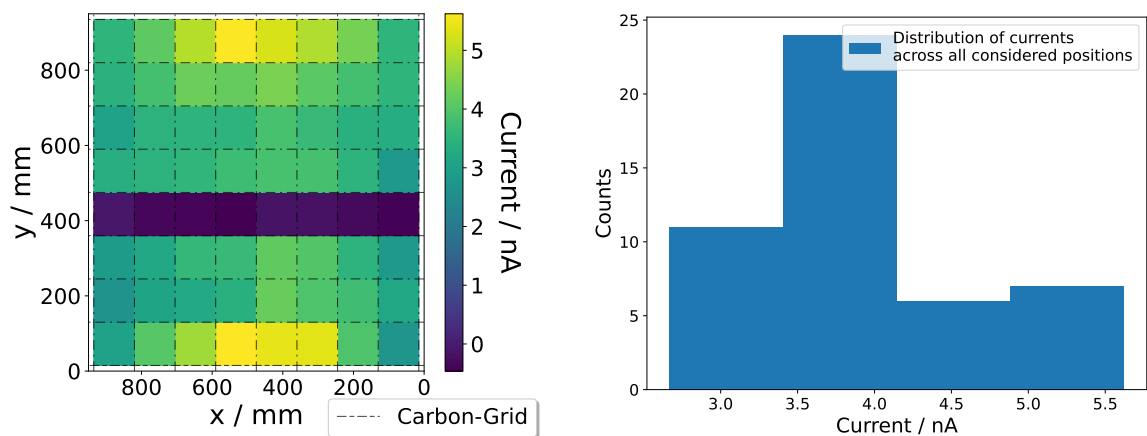(c) Measured current values with subtracted

Figure H.9: Plots showing the processing steps of the scan at 1870 V that result in figure 6.8

(a) Gain map showing the current at all positions considered in the uniformity calculations

(b) Histogram of all currents considered in the uniformity calculations

Figure H.10: Plots showing the data used in the uniformity calculations for the scan at 1870 V

Scan at 1930 V

(a) Raw data

(b) Baseline resulting from raw data

(c) Measured current values with subtracted

Figure H.11: Plots showing the processing steps of scan at 1930 V that then result in figure 6.8

(a) Gain map showing the current at all positions considered in the uniformity calculations

(b) Histogram of all currents considered in the uniformity calculations
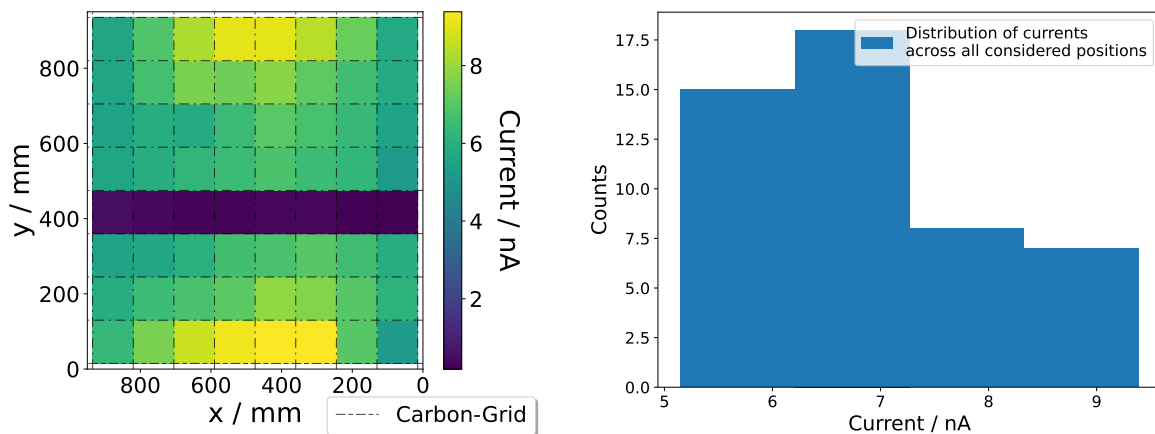
Figure H.12: Plots showing the data used in the uniformity calculations for scan at 1930 V
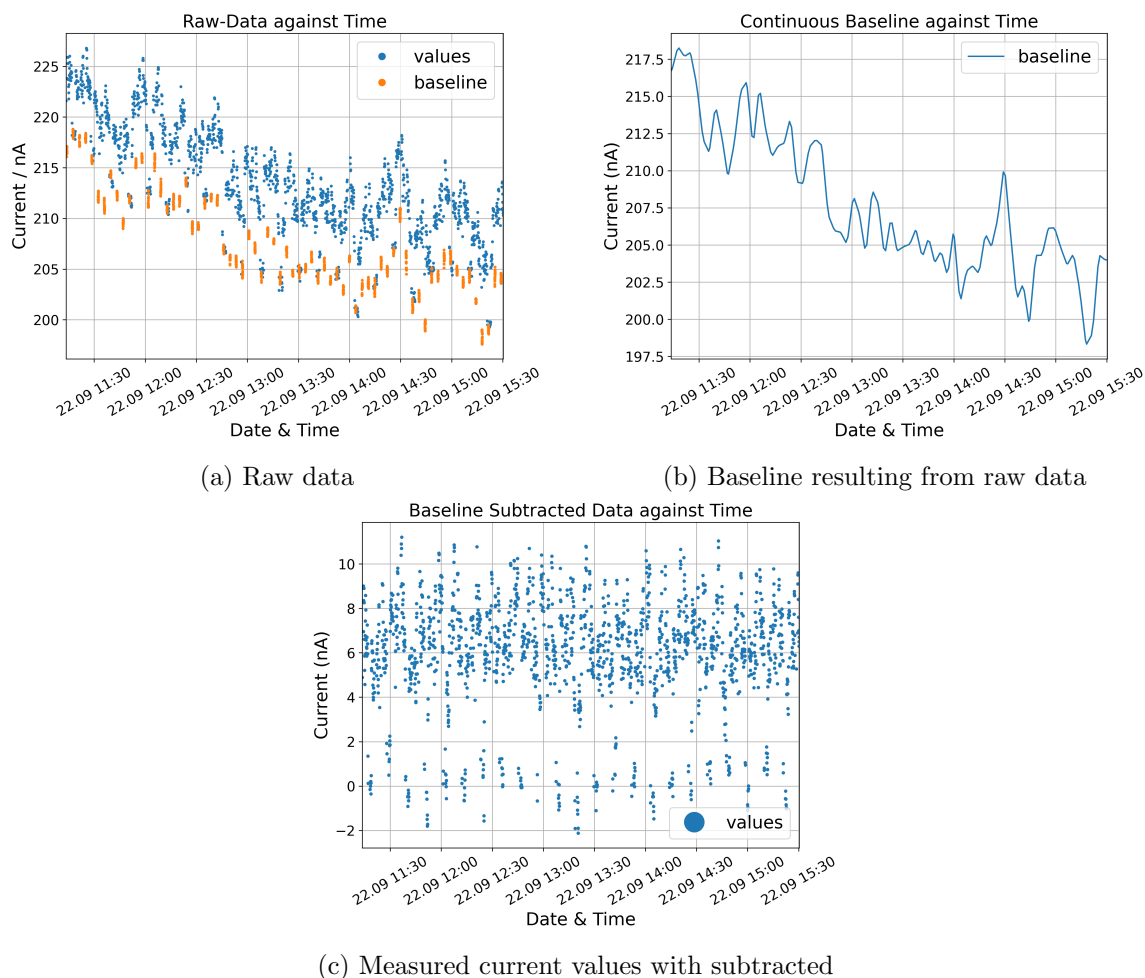
Scan at 1990 V

(a) Raw data

(b) Baseline resulting from raw data

(c) Measured current values with subtracted
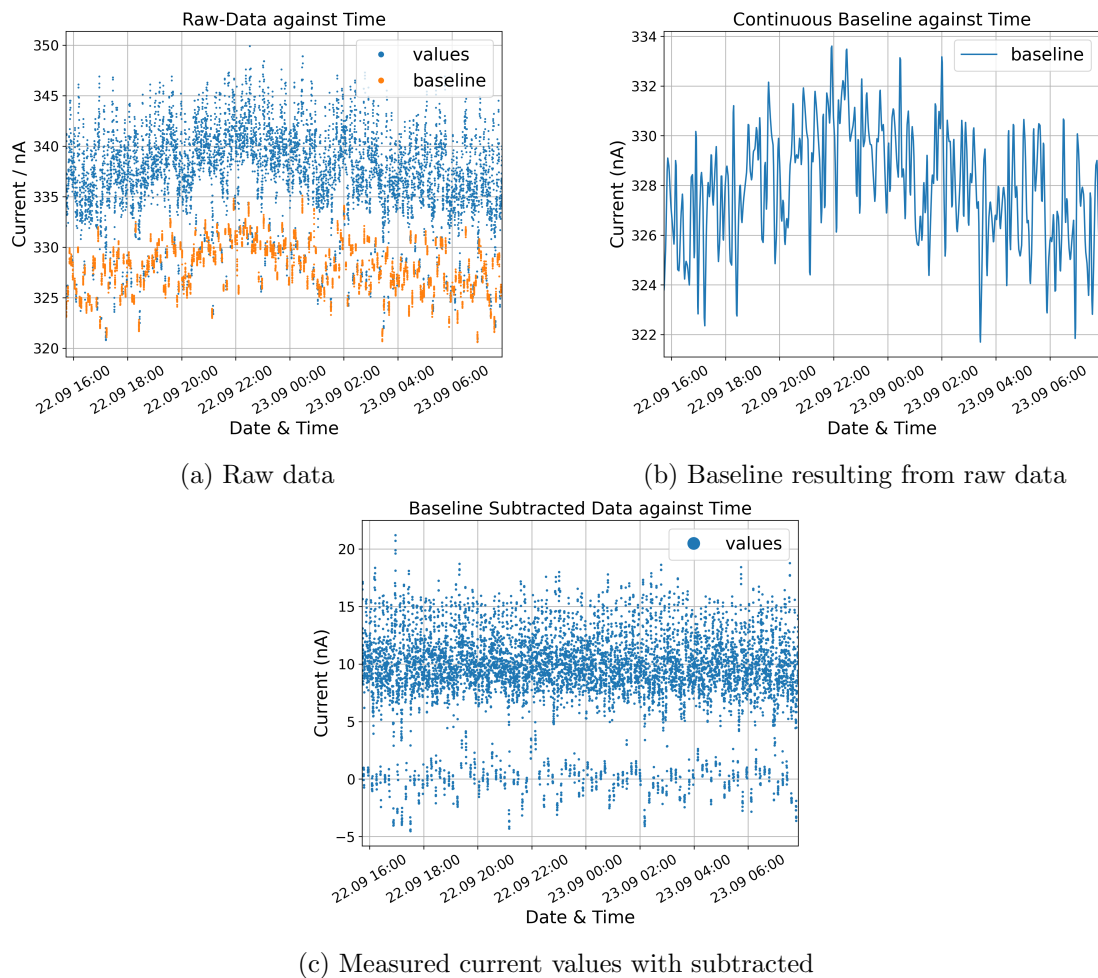
Figure H.13: Plots showing the processing steps of scan at 1990 V that then result in figure 6.8

(a) Gain map showing the current at all positions considered in the uniformity calculations

(b) Histogram of all currents considered in the uniformity calculations
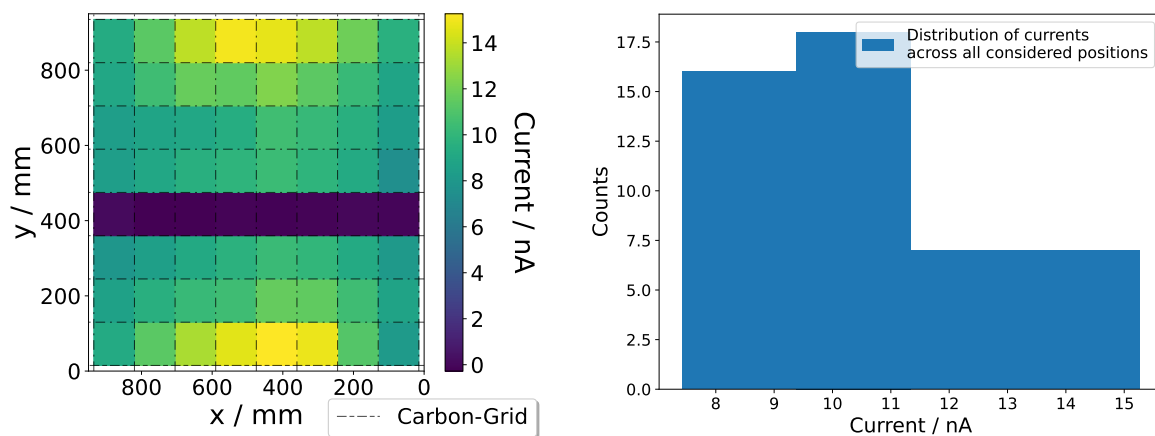
Figure H.14: Plots showing the data used in the uniformity calculations for scan at 1990 V

Bibliography

[1]   GSI Helmholtzzentrum für Schwerionenforschung. *The Accelerator Facility*. `https://` `www.gsi.de/en/researchaccelerators/fair/the_machine`. FAIR will be one of the largest and most complex accelerator facilities in the world, capable of providing particle beams of all chemical elements as well as antiprotons. 2023.

[2]   GSI Helmholtzzentrum für Schwerionenforschung. *Compressed Baryonic Matter*. `https:` `//www.gsi.de/work/forschung/cbmnqm/cbm`. 2023.

[3]   Christian Sturm. *The CBM Experiment at FAIR - towards commissioning in 2027*. Presentation. GSI / CBM Collaboration, 2023.

[4]   K.P. Schäfers et al. "1.10 - High-Resolution Small Animal Imaging". In: *Comprehensive Biomedical Physics*. Ed. by Anders Brahme. Oxford: Elsevier, 2014, pp. 181–211. ISBN: 978-0-444-53633-4. DOI: `https://doi.org/10.1016/B978-0-444-53632-7.00110-6`. URL: `https://www.sciencedirect.com/science/article/pii/B9780444536327001106`.

[5]   Wolfgang Demtröder. *Experimentalphysik 4*. Springer, 2010.

[6]   National Institute of Standards and Technology. *X-ray Mass Attenuation Coefficients*. `https://www.nist.gov/pml/x-ray-mass-attenuation-coefficients`. Accessed: 2023-10-08. 2023.

[7]   Hermann Kolanoski and Norbert Wermes. *Teilchendetektoren*. Springer, 2016.

[8]   Christoph Blume et al. *The Transition Radiation Detector of the CBM Experiment at FAIR: Technical Design Report for the CBM Transition Radiation Detector (TRD)*. Tech. rep. Collaboration FAIR: CBM, 2018.

[9]   Johannes Beckhoff. *Automated Test Stand Setup and Signal Reconstruction for the CBM-TRD*. Master's thesis. 2018.

[10] KOBOLD Messring GmbH. *Variable Area Flow Meter - Plastic - Low Flow KFR*. `https://www.kobold.com/Variable-Area-Flowmeter-Plastic-Low-Flow-KFR`. Acessed: 2023-09-08.

[11] G Rollmann. *Calculation of correction factors for variable area flow meters at deviating working conditions*. `https://www.kt-flow.de/wp-content/uploads/2019/10/korrekturfaktorenberechnung_en_2.3.pdf`. Accessed: 2023-09-08.

[12]   M.J. Berger et al. *Stopping-Power & Range Tables for Electrons, Protons, and Helium Ions*. `https://physics.nist.gov/cgi-bin/Star/compos.pl`. Accessed: 2023-09-15. National Institute of Standards and Technology, 2017.

[13]   National Institute of Standards and Technology. *NIST Chemistry WebBook, SRD 69*. `https://webbook.nist.gov/chemistry/`. Accessed: 2023-09-15. DOI: `DOI:https://doi.org/10.18434/T4D303`.

[14]   C. Fiorini et al. "A Monolithic Array of 77 Silicon Drift Detectors for X-Ray Spectroscopy and Gamma-Ray Imaging Applications". In: *Nuclear Science, IEEE Transactions on* 52 (Sept. 2005), pp. 1165–1170. DOI: `10.1109/TNS.2005.852727`.

[15]   Marie-Martine Bé et al. *Table of radionuclides (Vol. 3-A= 3 to 244)*. 2006.

[16]   iseg Spezialelektronik GmbH. *Technical documentation - EHS Series*. Tech. rep. July 2023.

[17]   CNC-Step GmbH Co. KG. *Betriebsanleitung High-Z T-Serie Rev. 1.7 FaceLift2021*. `https://www.cnc-step.de/wp-content/uploads/2022-02-23-Betriebsanleitung-High-Z-T-Serie_DE_.pdf`. Accessed: 2023-10-08. 2022.

[18]   Burkhard Lewetz. *CNC-Control Achscontroller CNCCON S*. `https://www.cnc-step.de/wp-content/uploads/CncconSBedAnlOhneHerstErkl-2.pdf`. Accessed: 2023-10-08. 2003.

[19]   scipy.linalg.lstsq. *Scipy 1.10.1 Manual*. `https://docs.scipy.org/doc/scipy/reference/generated/scipy.linalg.lstsq.html`.

[20]   scipy.optimize.curvefit. *Scipy 1.11.2 Manual*. `https://docs.scipy.org/doc/scipy/reference/generated/scipy.optimize.curve_fit.html`.

[21]   Luisa Faber. *Entwicklung und Inbetriebnahme eines Gassystems zu Untersuchung einer CBM-TRD Kammer unter Gasfluss*. Bachelor's thesis. 2021.

[22]   Marilyn MInus and Satish Kumar. "The processing, properties, and structure of carbon fibers". In: *Jom* 57 (2005), pp. 52–58.

[23]   Wolfram Mathworld. *Circle-Circle Intersection*. `https://mathworld.wolfram.com/Circle-CircleIntersection.html`. Accessed: 2023-08-10.

[24]   Philipp Kähler. *Private conversation*. 2023.

[25]   Hervé Abdi. "Coefficient of variation". In: *Encyclopedia of research design* 1.5 (2010).

[26]   Rainer Goebel. *Spatial Transformation Matrices*. `https://www.brainvoyager.com/bv/doc/UsersGuide/CoordsAndTransforms/SpatialTransformationMatrices.html`. Accessed = 2023-10-08. 2020.

[27]   International Organization for Standardization. *Uncertainty of measurement-Part 3: Guide to the expression of uncertainty in measurement (GUM: 1995)*. ISO, 2008.